



# Hydrodynamic Variability of an Intermittently Closed Estuary over Interannual, Seasonal, Fortnightly, and Tidal Timescales

Madeleine E. Harvey<sup>1,2</sup> · Sarah N. Giddings<sup>1</sup> · Geno Pawlak<sup>1,3</sup> · Jeffrey A. Crooks<sup>1,4</sup>

Received: 29 July 2020 / Revised: 5 October 2021 / Accepted: 6 October 2021 / Published online: 20 September 2022  
© The Author(s) 2022

## Abstract

Small low-inflow intermittently closed estuaries are common in Mediterranean climates worldwide; however, despite their important contributions to ecosystem services and coastal resilience, their dynamics have been less well studied relative to classical (i.e., deeper, persistent freshwater inflow) estuaries. It is known that infragravity wave propagation into these estuaries can induce strong currents and that closures lead to stagnating flows and declining water quality; however, how the estuarine circulation (tidal and subtidal) dynamically drives and responds to these conditions remains largely unknown. Here we analyze over 4 years of hydrodynamic observations in Los Peñasquitos Lagoon, a low-inflow, intermittently closed estuary in Southern California, to examine wave propagation into the estuary, sill accretion, and the estuarine circulation response over tidal, fortnightly, seasonal, and interannual time scales, providing an unprecedented view as to how these systems respond to changing forcing. Wave observations near the estuary inlet show that wave energy inside the inlet, which contributes to sill accretion, is dependent on water level relative to the sill height and has a tidal variation due to wave-current interactions. Tidal phase averages of conditions during open, pre-closure, spring, neap, and closed conditions highlight the large dynamic range that these estuaries experience. During open, low sill conditions, circulation and stratification are consistent with stratification-induced periodic straining and subtidal exchange varies with the fortnightly cycle as observed in many classical estuaries. However, as the sill grows, tidal circulation weakens and becomes strongly sheared and the subtidal exchange no longer scales with a classical theoretical pressure-friction balance.

**Keywords** Bar-built estuaries · Low-inflow estuaries · Intermittently closed estuaries · Intermittently closed/open lakes and lagoons

## Introduction

Low-inflow estuaries (LIEs) are estuaries where the total freshwater inflow is small, episodic, and/or seasonal, and they are commonly found in steep watersheds and

Mediterranean climates (Largier et al. 1997, 2013; Nidzieko and Monismith 2013). As a result, their density structure and circulation can differ substantially from theory developed for estuaries with consistent and larger river discharge. Here we refer to the latter as “classical” estuaries, which are typically partially- to well-mixed, salinity dominates density and decreases with distance from the ocean, and the resulting subtidal exchange flow is into the estuary at depth and out at the surface (e.g., Geyer and MacCready 2014). In contrast, LIEs can exhibit reduced density gradients which can stagnate the exchange flow. At times temperature can dominate the density gradients (termed a thermal estuary), and they can even become hypersaline during the dry season, leading to inverse exchange flow (in at the surface, out at depth) (Largier et al. 2010). Urban runoff or upstream dam releases may be strong enough to suppress hypersalinity development in some estuaries that historically functioned as LIEs (Largier et al. 1997).

Communicated by Neil Kamal Ganju

✉ Madeleine E. Harvey  
meharvey@ucsd.edu

<sup>1</sup> Scripps Institution of Oceanography, University of California San Diego, 9500 Gilman Dr, La Jolla, CA 92093-0206, USA

<sup>2</sup> Naval Undersea Warfare Center, 1176 Howell Street, Newport, RI 02841, USA

<sup>3</sup> Mechanical and Aerospace Engineering, University of California San Diego, 9500 Gilman Dr, La Jolla, CA 92093-0411, USA

<sup>4</sup> Tijuana River National Estuarine Research Reserve, 301 Caspian Way, Imperial Beach, CA 91932, USA

Bar-built estuaries broadly defined are those where sandbars or barrier islands are built up by ocean waves and currents. In this paper, we will use the term bar-built estuary (BBE) to refer to a subset of these estuaries sometimes called restricted mouth estuaries that are small LIEs with only one inflowing river and one connection to the ocean, consistent with the use of this term in Clark and O'Connor (2019), and thus differentiating the BBEs discussed here from those that exist along coastlines with barrier islands often with multiple inlets such as those found along the US Gulf Coast, US East coast, and the Netherlands. BBEs included here are generally small, shallow systems with narrow tidal inlets (estuary mouth, cross-sectional area on the order of 100 m<sup>2</sup> or less) (Ranasinghe and Pattiaratchi 2003) that experience rapid morphological changes. They are common on wave-dominant coasts with seasonal rainfall and microtidal (Cooper 2001; Davidson et al. 2009) or mesotidal (Behrens et al. 2013; Rich and Keller 2013) ranges. These BBEs can be found worldwide including along the coasts of California (Largier et al. 1997, 2013; Nidzicko and Monismith 2013), Spain (Moreno et al. 2010), Portugal (Dodet et al. 2013; Bertin et al. 2019), Australia (Ranasinghe and Pattiaratchi 1999a, b; Roy et al. 2001; Gale et al. 2007; McSweeney et al. 2017), South Africa (Clark and O'Connor 2019; Largier et al. 2019), and Chile (Dussailant et al. 2009). In restricted mouth BBEs, flood tides, waves, and wave-current interactions drive alongshore and cross-shore sediment transport into tidal inlets forming a sill comprised of sand and cobbles while ebb tides and fluvial events drive transport out of these inlets (Ranasinghe et al. 1999; Behrens et al. 2013; Rich and Keller 2013; Orescanin and Scooler 2018). The waves and sill height can have profound impacts on the circulation, inundation, stratification, and dissolved oxygen in these estuaries (Largier et al. 1992; Gale et al. 2007; Cousins et al. 2010; Behrens et al. 2016) that further differentiate these from classical estuarine theory. In some restricted mouth BBEs, the dynamic inlet morphology can occasionally lead to inlet closures when the sill is high enough to block tidal exchange with the ocean, in which case they are termed intermittently closed estuaries (ICEs) or intermittently closed/open lakes and lagoons (ICOLLs, e.g., McSweeney et al. 2017), the former used here.

The interactions between offshore waves propagating into inlets and tidal currents in the inlet area are critical to both sill build-up and estuary dynamics in BBEs and ICEs. These wave-current interactions can impact the amount of wave energy in the inlet where sea and swell waves are able to propagate into the inlet during flood tides but can be blocked by ebb tides (Ranasinghe et al. 1999; Behrens et al. 2013; Rich and Keller 2013; Orescanin and Scooler 2018; Orescanin et al. 2014). Wave radiation stress gradients can induce a water level set up within single-inlet estuaries (Olabarrieta et al. 2011; Dodet et al. 2013). Recent work has focused

on the influence of infragravity (IG hereafter) waves on sediment transport within tidal inlets (Dodet et al. 2013; Bertin et al. 2019, 2018). Multiple ICE observational studies and numerical simulations (XBeach) have shown that the strength of IG motions is correlated with offshore wave heights, and that the IG energy depends on the tidal phase and connectivity between the ocean and estuary (Williams and Stacey 2016; McSweeney et al. 2020; Bertin and Olabarrieta 2016). Additionally, observations have found that the magnitude of IG orbital motions can be on the same order as tidal velocities (Uncles et al. 2014; Williams and Stacey 2016; Bertin and Olabarrieta 2016). Bertin et al. (2019) found that in storm wave conditions during flood tides, peaks in along-stream velocity currents occurred during the passage of IG wave crests and currents were reduced or reversed during the passage of troughs. Instantaneous sand fluxes increased up to 2 orders of magnitude during IG wave crests, which contributed to inlet accretion. In a Central California ICE, IG energy was only seen in the system just before closure when the river flow decreased in magnitude (Orescanin and Scooler 2018).

The impact of inlet closures on navigation and water quality has motivated much of the research in BBEs, particularly ICEs, to address closure mechanisms (Ranasinghe and Pattiaratchi 1999a; Roy et al. 2001; Gale et al. 2007). Less work has focused on the hydrodynamics of LIEs, BBEs, and ICEs. Some studies have examined the open inlet periods including the influence of tides and stratification (Largier 1986; Largier and Taljaard 1991; Ranasinghe and Pattiaratchi 2003; Gale et al. 2006, 2007). A few studies have examined the sill's impact on the dynamic connection to the ocean (Williams and Stacey 2016) and on the hydrodynamics during closed periods (Hayes 1979; Williams 2014; Behrens et al. 2016). In mesotidal restricted mouth BBEs, the estuary tidal range depends on both the offshore tidal range and the sill height and location. During the flooding higher tides, the estuary and ocean water levels are approximately the same, allowing for connection between the nearshore ocean and estuarine environments. As the tide falls to its daily lower-low, the ocean retreats below the perched estuary inlet and the nearshore ocean dynamically disconnects from the estuary (Williams and Stacey 2016). While these contributions have provided valuable insights into the hydrodynamics of these systems, the vertical structure, subtidal, and temporal variability of the estuarine circulation have remained unresolved. Moreover, although prior work has suggested that classical estuarine theory may still apply in LIEs at least part of the time given that they experience strong density gradients (e.g., Winant and Velasco 2003), ICE circulation has not been compared to estuarine theories (e.g., MacCready and Geyer 2010; Geyer and MacCready 2014).

The hydrodynamics of restricted mouth BBEs and ICEs have historically been under-studied, potentially because the shallow waters and wave activity near the inlet have

prevented these systems from being used as ports and harbors without dredging and/or armoring (Williams and Stacey 2016). Yet understanding their hydrodynamics is critical for understanding their critical ecosystem services and resilience to future changes including development, upstream freshwater diversions, and climate change. These estuaries can support extensive marsh, tidal flat, and subtidal habitats, provide carbon sequestration, confer resilience to flooding from storms and sea level rise, and are valuable recreational spaces (Zedler and Kercher 2005; Shepard et al. 2011; Bouma et al. 2014; Holmquist et al. 2018; Rezaie et al. 2020). However, their dynamics can lead to development of low dissolved oxygen, stagnation, and outbreaks of mosquitos carrying vector-borne diseases, and other deleterious ecosystem consequences. This paper uses extensive field observations from Los Peñasquitos Lagoon (LPL) in Southern California (Fig. 1) to explore how the dynamics of a small, shallow, bar-built, intermittently closed estuary changes over various time scales. This includes examining the dynamical interaction between waves, sill height, and estuarine circulation. We also address the impacts of these dynamics on dissolved oxygen.

Observations in LPL from December 2014 through mid June 2019 of physical parameters including water level, waves, bathymetry, currents, salinity, temperature, density, and dissolved oxygen are used here (Fig. 2). Few long-term data sets in small systems such as LPL exist, with the notable exception of a study in Elkhorn Slough, a small Central California LIE that is open year-round and develops an inverse circulation during the summer and fall months (Nidzieko and Monismith 2013). The long time period allows us to examine estuarine dynamics not just through a few tidal cycles, but over a range of conditions and timescales, thus providing a broader understanding of the estuarine dynamics and its response to and dynamical feedbacks with varying climatological and morphological states. Specifically, the observational period covers a few unique Southern California climatological periods including a marine heatwave, a large El Niño, and anomalously wet and dry years. Morphological states span open and scoured to closed, high-berm mouth conditions. Thus, we are able to provide new insights into the dynamics of small, shallow, ICEs and how they change over various time scales including tidal, diurnal, spring-neap, seasonal, and interannual. This type of long-term dataset can provide baseline dynamical understanding

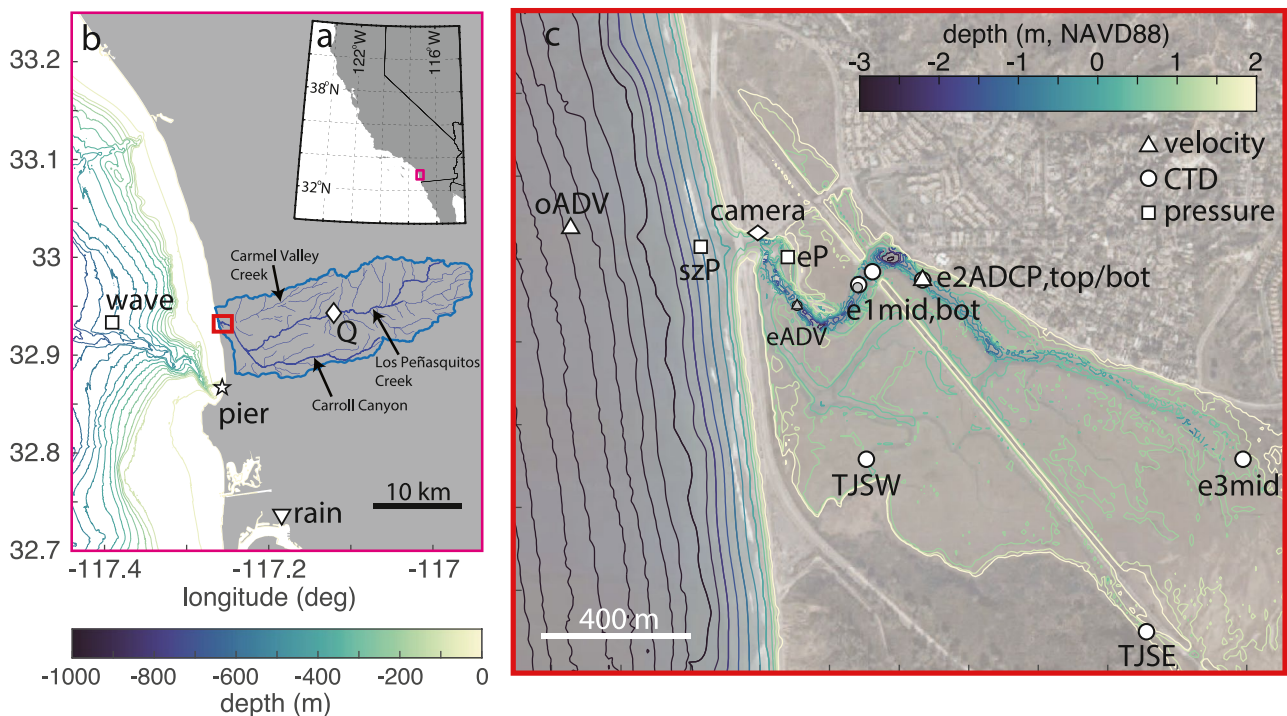


**Fig. 1** Location of Los Peñasquitos Lagoon and instruments deployed. **a** California coastline with outline of panel **b** delineated in pink. **b** San Diego County coastline with watershed of Los Peñasquitos Lagoon and offshore bathymetry. USGS river discharge gauge ( $Q$ ) denoted as a diamond; SIO Pier (pier) denoted as a star; CDIP wave buoy 100 (wave) denoted as a square; and NCDC precipitation gauge (rain) denoted as an inverse triangle. Red outline delineates the region

of **c**. **c** Los Peñasquitos Lagoon with instrument locations (white for nearly continuous measurements, gray for short-term deployments) overlain on marsh topography and bathymetry in teal (light colors are higher elevation). Estuary bathymetry was collected from a combination of UAV measurements and towed ADCP measurements, while those offshore are from the 1/3 arc-second San Diego Coastal DEM model from NOAA and all are referenced to NAVD88

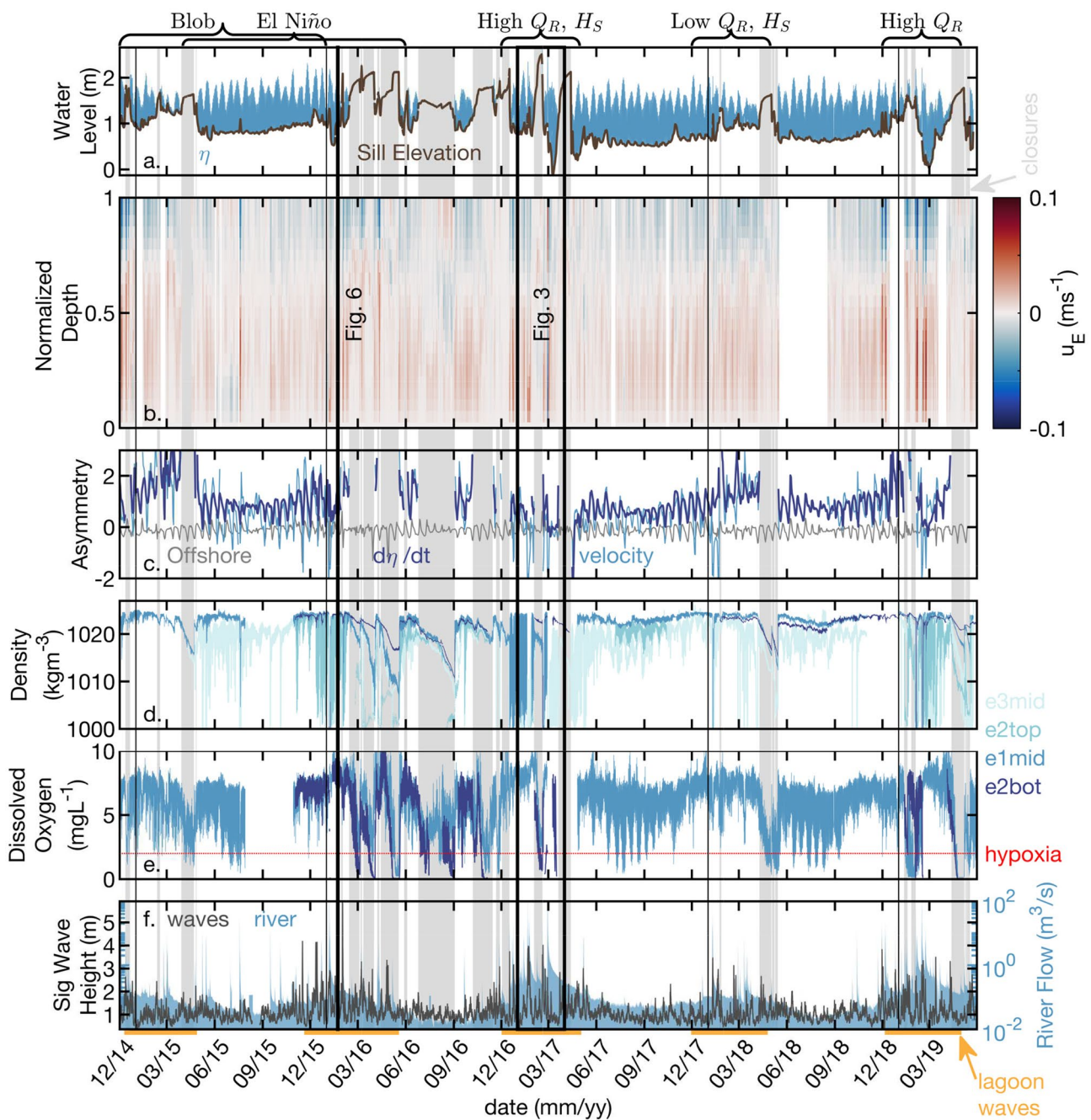


**Fig. 2** Los Peñasquitos data from 01 December 2014 to 31 May 2019. Gray vertical bars indicate periods of inlet closure. **a** Water level (m, NAVD88, dark blue) and lower-lower water level indicating the sill height (m, NAVD88 brown). **b** Exchange velocity defined as the subtidal velocity minus the EOF1 mode 1 velocity,  $u_E^{obs}(t, \sigma) = \langle u \rangle - EOF1$  ( $m s^{-1}$ ). **c** Water level ( $\gamma_0^{o,\delta\eta/\delta t}$  gray;  $\gamma_0^{e,\delta\eta/\delta t}$ , dark blue) and velocity ( $\gamma_0^{e,u}$ , medium blue) asymmetry in the estuary (*e*, blues) and offshore (*o*, gray). Asymmetry in the estuary is not calculated during periods of closure. **d** Density at e2top (near-surface, light

blue), e1mid (mid-water column, medium blue), e2bot (near-bottom, dark blue) and e3mid (furthest upstream, very light blue) locations. **e** Dissolved oxygen at e2bot (dark blue) and e1mid (medium blue) sensors. **f** Significant wave height from Torrey Pines Outer Buoy (dark gray, CDIP Buoy #100) and river flow (filled medium blue, 158% USGS gauge 11023340). Dark grey vertical lines indicate January 1 of each year, black rectangles indicate time periods shown in Figs. 3 and 6 as labeled, and orange bars indicate time periods when wave data was collected at oADV, szP, and eP

to interpret potential responses to future changing forcing conditions. After describing our methods (see the “Methods” section), we describe the long-term trends in circulation,

the wave forcing that propagates into the system, the tidal circulation with different sill heights, the circulation over a fortnightly spring-neap cycle, and impacts on dissolved

oxygen conditions (see “Results” section). We then discuss how the interannual forcing variability affects the estuary inlet morphodynamics, how those changes affect the tidal circulation, and finally how they affect the residual circulation, including comparing the observed dynamics to classical estuarine theory (see the “Discussion” section).

## Methods

### Field Site Description: Los Peñasquitos Lagoon

Between December 2014 and June 2019, measurements were conducted in LPL, a small ICE in Southern California (Fig. 1). LPL is an LIE, located in a Mediterranean climate with minimal precipitation during the summer and episodic inputs during the winter. LPL serves as the outlet to a 255 km<sup>2</sup> watershed draining Carmel Valley, Los Peñasquitos Canyon, and Carroll Canyon. The estuary is a designated Natural Marsh Preserve by the state of California and is part of the Torrey Pines State Reserve. LPL is small and shallow (max depth less than 4 m), covering approximately 2 km<sup>2</sup> with extensive marsh habitat (Fig. 1). The main channel is about 2.5 km long and less than 70 m wide. The estuary inlet crosses a nourished sand and cobble beach where adjacent beach sand accretes in the summer and erodes in the winter (Ludka et al. 2016) while the inlet experiences accretion during winters (Harvey et al. 2020; Young et al. 2018). The last major beach nourishment was in 2001, large nourishments further north in 2012 are hypothesized to have increased sand volumes at the LPL mouth in 2013, and minor nourishments occur every year during inlet dredging (SANDAG 2018; Crooks et al. 2014).

LPL has been subjected to physical modifications in and around the estuary which impact its hydrodynamics and connectivity with the ocean. Microfossil, pollen, and sediment data from deep cores demonstrate a rapid increase in sedimentation and infilling of the lagoon beginning in the early nineteenth century, likely related to cattle grazing and increased erosion in the watershed (Cole and Wahl 2000; Scott et al. 2011). In 1925, a railway berm was relocated to the middle of the estuary and in 1933 Highway 101 (now Torrey Pines Road) was completed upon a berm along the ocean edge of the estuary (Beller et al. 2014). From 2015 to 2017, three wooden railway trestle bridges were replaced with concrete bridges. Over the main span, a bridge with about 96 timber pilings was replaced with a concrete bridge with 27 concrete pilings. Historically, the inlet location was able to migrate along the coast; however, during the Highway 101 construction, the inlet was moved approximately 0.5 km south of its 1932 location and constricted to a bridge opening. The bridge was rebuilt in 2004–2005 leading to the

current 38-m-wide constricted inlet. While LPL was historically an LIE with hypersaline conditions likely developing during late summer and fall, increased freshwater runoff from urban development (White and Greer 2006) prevents the main channel from becoming hypersaline (Largier et al. 1997) although smaller arms do continue to become seasonally hypersaline. Moreover, construction of an upstream dam and water impoundments has decreased winter time river flows (Henning et al. 2012).

Inferences from historical records, vegetation surveys, and marsh sediments indicate that LPL began to experience increasing periods of mouth closure associated with these anthropogenic impacts (Purer 1942; Cole and Wahl 2000; Scott et al. 2011; Hastings and Elwany 2012; Beller et al. 2014). The inlet is frequently dredged (Hastings and Elwany 2012) in response to a combination of potential for vector-borne disease, flooding, and low dissolved oxygen costing approximately \$115,000 to \$130,000 for each dredging event (Mike Hastings, personal communication). A major estuarine restoration is proposed for the coming years (LPL Foundation et al. 2016).

## Observations

### Velocity Measurements

A long-term mooring ~0.75 km upstream from the inlet (e2, Fig. 1) with an upward-looking 1200-kHz acoustic Doppler current profiler (ADCP, RDI Workhorse Monitor) sampling at 0.5 Hz in mode 12 (rapid ping mode with sub-pings) was deployed on a bottom-mounted flat plate measuring velocity in 10 to 20 cm bins with varying blanking distances of 0 to 15 cm collecting data in either beam (01 December 2014 to 17 February 2015) or earth coordinates (26 February 2015 to 14 June 2019). The ADCP was swapped every 2–3 months collecting a nearly continuous record from 01 December 2014 until 14 June 2019. Due to deployment logistics, the exact location and depth of each deployment varied slightly. They were adjusted to a consistent depth by aligning them to survey-located pressure sensors at e1 or eP (described below).

Individual velocity measurements were ensemble averaged into 10-min bins, resulting in errors of 0.67 cm s<sup>-1</sup> or less for all but one 1-month deployment (which had an error of 0.80 cm s<sup>-1</sup>). For each deployment, velocities were rotated into principal axis coordinates based on each deployment's maximum variance during open periods in order to define along and across-channel axes ( $u$ ,  $v$  respectively). Velocities were transformed into depth-normalized coordinates ( $\sigma = z/D$ ), where  $D$  is the instantaneous, time-varying, water depth. Velocities were extrapolated to the bed (assuming no flow at the bed and interpolated using a shape-preserving piecewise cubic

interpolation) and surface (using a quadratic extraction that assumes  $\frac{\partial u}{\partial z} = 0$  at the surface) following Giddings et al. (2014). Gray thatched areas on figures with depth-varying velocity indicate extrapolated data.

### CTD and Turbidity Measurements

Adjacent to the ADCP at e2 (Fig. 1), near-surface (mounted just beneath a floating buoy) and near-bottom conductivity, temperature, and depth sensors (CTD, SBE-37 SMP) sampling at 1 min and 2 min (5 min after June 2017), respectively, were deployed (Fig. 2d, light and dark blue). Near-bottom CTD measurements were initially on the bed and moved to ~20 cm above the bed after January 2019. Dissolved oxygen (DO) measurements were collected using a CTD-integrated SBE-63 optical dissolved oxygen sensor at the bed from 03 November 2015 to 09 October 2017 and 10 January 2019 to 20 June 2019 (Fig. 2e) and at the surface between 10 January 2019 and 2 April 2019. The CTDs occasionally experienced significant biofouling and/or sediment entrainment resulting in artificially low salinity measurements. Unrealistic data was removed from all analyses. In some cases, the instrument was not obviously fouled; however, data was questionable and is denoted by a dashed line in Fig. 2d. Surface and bottom density measurements were used to estimate the Brunt–Väisälä frequency,  $N^2 = -\frac{g}{\rho_o} \frac{\Delta\rho}{\Delta z}$ , using bulk top to bottom stratification ( $\Delta\rho$  over a height of  $\Delta z$ ) where  $\rho_o$  is the average density and  $g$  is gravity.

In addition to the moorings, four CTD-DO instruments with turbidity and pH (YSI EXO dataSondes) were deployed on poles by the Tijuana River National Estuarine Research Reserve (TRNERR) System Wide Monitoring Program (SWMP), fixed at approximately 0.5 m above the bed (i.e., mid-water column) sampling at 15-min intervals. The YSI EXO turbidity sensors are lab-calibrated with a 2-point calibration using DI water and a 126 NTU standard such that their output is in NTU. Occasional spikes (> 100 NTU) well outside the typical measurements (99.9% of all turbidity measurements fall beneath 14.3 NTU) are removed. Two instruments at e1 and e3 (downstream and upstream of our ADCP/CTD mooring respectively) were deployed in the main channel (Figs. 1 and 2d, medium blue, e1mid, and very light blue, e3mid) and two (TJSW and TJSE) were deployed in side arms. TJSE is not used in this manuscript and TJSW was discontinued on 02 July 2017. Due to bridge construction, the e1 sensor was moved ~50 m downstream on 29 October 2015 and was located about 0.75 m higher in the water column from 29 October 2015 to 27 February 2017. All data from e1mid will be analyzed as a mid-water column instrument; however, note that because it is fixed in elevation, its depth relative to the water surface and any pycnoclines changes with time. The absolute elevation

of e1 was obtained with a Spectra Precision Epoch 50. During 2 ~ 1-month gaps in the water elevation time series at e1 (September 2015 and March 2017), water levels were supplemented with ADCP pressure measurements. All data was interpolated to 10-min intervals.

### Wave Measurements

During each winter (approximately November through late March/early April, see orange bars on Fig. 2f), two buried Paroscientific, Inc. pressure sensors were deployed just offshore (in the surfzone, szP) and just inside of the estuary inlet (eP). Sensors were buried approximately 1 m under the sand, although sediment accreted and eroded throughout the deployment period. Sensor locations varied slightly year to year due to a mobile cobble layer restricting possible deployment locations. The exact locations of szP and eP were surveyed using a Spectra Precision Promark 700 Global Navigation Satellite System Real-Time Kinematic (GNSS RTK) GPS. In February 2016 and January 2017 sand at szP eroded more than about half a meter, and the sensor was relocated for public safety. eP was moved once on 17 March 2017 when accretion exceeded 1 m causing the sensor to no longer be in direct wave action. The pressure sensors sampled at 2 Hz continuously for 59.73 min each hour. szP and eP pressure measurements were corrected to account for frequency attenuation effects due to burial (Raubenheimer et al. 1998).

An acoustic Doppler velocimeter (ADV) was deployed just offshore of the LPL inlet in ~9-m water depth at oADV overlapping with the szP and eP winter deployments but extending longer in time, 6 months, deployed before and recovered after the szP and eP sensors. The upward facing ADV sampled velocity and pressure at 2 Hz at 0.5 to 0.9 m above the sand bed respectively.

Variance preserving spectra were computed for 30-min windows every 15 min from the pressure signals at oADV, szP, eP, and e2ADCP. Each 30-min window was divided into 11 segments with 75% overlap. Significant wave heights for total, swell, and IG bands ( $H_T$ ,  $H_{IG}$ , and  $H_{SW}$ ) were calculated according to:

$$H = 4 \times \sqrt{\int_{f_1}^{f_2} S(f) df} \quad (1)$$

where  $f$  is the frequency;  $S(f)$  is the power spectral density of the free surface,  $\eta$ ;  $f_1 = 0.167$  Hz,  $f_2 = 0.04$  Hz, (6 to 25 s periods) for swell energy; and  $f_1 = 0.04$  Hz,  $f_2 = 0.004$  Hz (25 to 250 s periods) for IG wave energy (Bertin et al. 2018).

A downward facing ADV sampling at 8 Hz at 0.28 m above the bed with an attached un-calibrated optical backscatter sensor (OBS) sampling at 0.67 m above the bed was

deployed for 1 day on 22 January 2016 near the estuary mouth (eADV).

### Meteorological Measurements

Atmospheric pressure was obtained from 3 stations: the TRNERR SWMP provided barometric pressure measurements at LPL (on land adjacent to e1 on Fig. 1c); a 2-Hz atmospheric pressure sensor was stationed at Scripps Institution of Oceanography (SIO, near location labeled pier on Fig. 1b); and a third barometric pressure sensor was provided by Earth Networks, Inc. from the SIO Pier (pier on Fig. 1b). All water level measurements were corrected with barometric pressure from one of these three sensors. Specifically, the offshore, surfzone, and mouth 2-Hz pressure sensors were always corrected with the 2-Hz SIO atmospheric pressure sensor. For all other instruments, further inside the lagoon, the TRNERR SWMP barometric pressure sensor was used when it was available and occasionally when it was not working, the Earth Networks, Inc. SIO Pier sensor was used. Earth Networks, Inc. also provided precipitation, air temperature, and wind data from the SIO Pier, approximately 7.5 km south of LPL (pier, Fig. 1b). Long-term precipitation records were obtained from the National Climatic Data Center (NCDC) Station USW00023188 at San Diego Airport, 26 km south of LPL (rain, Fig. 1b).

### Bathymetry

Bathymetric data within the estuary was collected in transects using a downward-looking, towed ADCP (see Fig. 1c). The depth was converted into absolute elevation by subtracting the depth data from the surveyed water level sensor. Bathymetric transects were conducted on 11 January 2015, 12 January 2016, and 29 January 2016 upstream of the railroad bridge and on 03 March 2017, 13 March 2017, 27 March 2017, and 04 April 2017 downstream of the bridge. Additionally, depth measurements from occasional CTD casts were incorporated into the channel depth bathymetry dataset. Shallower (intertidal) elevations near the mouth were collected from unmanned aerial vehicle (UAV) data converted into elevation with structure-from-motion software (Pix4D). The composite bathymetry (Fig. 1c) shows a relatively uniform, shallow channel which decreases in depth upstream with a sill near the mouth and two deeper holes near the outside of the two sharpest bends. Harvey et al. (2020) showed that the lower-low water levels in the estuary provided a good approximation of the average elevation of the inlet (measured through bathymetry and topography surveys). As such, the sill elevation,  $h_{\text{sill}}$ , is defined as the lower-low water level at e1. During prolonged closures, the sill elevation may increase due to additional sediment delivery by waves; however, we also observe a net increase in water

level during closures presumably due to a combination of sill elevation increases and continued freshwater inflow into the lagoon. We do not consider groundwater flow through the sill. Thus overall, the estimate provides a lower bound of sill height during closure and a good approximation of sill height and inlet state changes over time (Harvey et al. 2020).

### Additional Measurements

Ocean (o) water level, temperature, and salinity at SIO Pier were extracted from the NOAA tide gauge (station 9410230, [tidesandcurrents.noaa.gov](https://tidesandcurrents.noaa.gov)) and the Southern California Coastal Ocean Observing System (SCCOOS, [sccoos.org](https://sccoos.org)) Automated Shore Stations (Fig. 1b). Offshore wave data (significant wave height,  $H_{\text{sig}}$ ; peak period; and peak direction) was extracted from the Coastal Data Information Program (CDIP, [cdip.ucsd.edu](https://cdip.ucsd.edu)) Torrey Pines Outer Buoy 100, 12 km west (offshore) of the inlet (Fig. 1b).

River discharge is estimated from the United States Geological Survey (USGS) Los Peñasquitos Creek Gauge 11023340 (Fig. 1b). Using Elwany's (2011) calculations and gauged watershed areas suggest that the continuous Los Peñasquitos Creek USGS gauge reported values should be multiplied by 158% to approximate the total river inflow.

A time-lapse camera taking photos of the inlet area during daylight every 15 min was deployed near the mouth by the TRNERR SWMP (Fig. 1c).

### Analysis Methods

#### Removal of Tides

Velocities were low-pass filtered using a Godin filter (Godin 1972; Thomson and Emery 2014) to remove tidal energy. A Godin filter specifically removes energy at the diurnal tidal constituent frequency (and higher), while keeping longer tidal interaction periods such as the fortnightly spring/neap cycle. Walters and Heston (1982) and Thompson (1983) both point to the superior ability of a Godin filter to remove tidal components over cosine-Lanczos and cosine-Lanczos squared filters, as we also found. However, they also point out that the Godin filter can attenuate 2–3 day variations in surface elevation. Given our focus on tidal variation, and subtidal variations over fortnightly and longer timescales, results presented here are insensitive to the filter choice and we chose the Godin filter due to its ability to remove diurnal tidal motions. Data that has been subtidally filtered is denoted with angled brackets,  $\langle \bullet \rangle$ .

#### Empirical Orthogonal Functions

Singular value decomposition (SVD) (Thomson and Emery 2014) of the low-passed velocities was used to

calculate the first three empirical orthogonal function modes (EOF1, EOF2, and EOF3). These are used below to estimate the subtidal exchange velocity.

**Asymmetry**

Asymmetry can be an important parameter for sediment transport into or out of an inlet. The asymmetry can be defined in several ways including inlet asymmetry and tidal asymmetry, and is often quantified by a normalized skewness (Thomson and Emery 2014; Nidzieko 2010). In order to better incorporate sediment transport which is generally proportional to velocity cubed (Bagnold 1966), Nidzieko and Ralston (2012) define  $\gamma_0$  as the third sample moment about zero normalized by the second sample moment about zero (Eq. 2). The skewness was calculated using the free surface to compare measurements in the estuary and in the ocean and using the velocity in the estuary to better assess the contributions of skewness to sediment transport. To construct a time series, a running window of 2 times a lunar day (24.84 h) is used where the lunar day starts on an offshore higher-high water (HHW).

$$\gamma_0 \equiv \frac{\mu_3}{\mu_2^{3/2}} = \frac{\frac{1}{n-1} \sum_{i=1}^n (F_i)^3}{\left(\frac{1}{n-1} \sum_{i=1}^n (F_i)^2\right)^{3/2}} \tag{2}$$

where  $n$  is the number of samples  $F_i$ . For  $\gamma_0^{o,\delta\eta/\delta t}$ ,  $F$  is defined as  $\delta\eta_o/\delta t$  where  $\eta_o$  is the offshore water level. For  $\gamma_0^{e,\delta\eta/\delta t}$ ,  $F$  is defined as  $\delta\eta_e/\delta t$  where  $\eta_e$  is the estuary water level. For  $\gamma_0^{e,u}$ ,  $F$  is defined as the depth-averaged along-stream estuarine velocity,  $[u]$ , (square-brackets indicate depth-averaged).

The tidal asymmetry factor of the inlet morphology is defined as  $\gamma_{inlet}$  (Friedrichs and Madsen 1992; Nidzieko 2010):

$$\gamma_{inlet} = (1 + \alpha) \frac{a}{\bar{d}} - \frac{b - B}{\underline{b}} \tag{3}$$

where  $a$  is the tidal amplitude (i.e., half the tidal range between MHHW and MLLW,  $a \sim 0.8$  m),  $\bar{d}$  is the mean estuary depth ( $\bar{d} \sim 1$  m),  $B$  is the main channel width (below MLLW),  $\underline{b}$  is mean of the total estuary width between MLLW and MHHW, and  $\alpha = 0.5$  is a weighted friction term following Nidzieko (2010).  $B \sim 35$  m and  $\underline{b} \sim 67.5$  m were approximated with drone imagery and based on distances in the inlet area near the mouth.

**Phase Averaging**

Various parameters were phase-averaged in order to examine consistently repeatable patterns. All variables were

interpolated or bin-averaged to 10-min intervals prior to phase averaging. Data was then tidal phase averaged and/or fortnightly phase averaged.

**Tidal Phase Averaging** Tidal phase averages are defined between two offshore higher-high water (HHW, defined as a high tide that is higher than the previous high tide) events in order to capture the mixed semi-diurnal tide. If there are two HHW events in a row, the segment is ignored. If there is a HHW followed by two lower high water (LHW) events, then that tidal segment is defined between the offshore HHW and the second LHW event (the time period between the second LHW and the next HHW is ignored). This results in 1796 individual semidiurnal tidal phase (HHW through LHW to the following HHW) realizations with an average length of 24.76 h. For the phase average plots and analyses, the phase is shifted such that zero phase is defined as the estuary depth-averaged, phase-averaged slack water preceding the offshore HHW water level during open conditions (a shift of a little more than  $\pi/3$  or 4.67 h before HHW). This eases description as a phase of  $\pi$  approximately denotes the transition from the larger to the smaller tide and  $\pi/2$  and  $3\pi/2$  approximately denote transitions from flood to ebb tides. The number of realizations of each variable is dependent on the data availability as most instruments had data gaps (Table 1). If more than 75% of a given tidal cycle is missing data, that tidal cycle was ignored and not included in the tidal phase average. Angle brackets with a  $\tau$  subscript indicate tidal phase averaging,  $\langle \bullet \rangle_\tau$ .

The tidal phase averages were performed for three separate inlet states: open, pre-closure, and closed. The open or closed inlet state was determined from estuary water levels (and

**Table 1** Average number of realizations that go into  $M_2$  phase averages in Figs. 7 and 8

Variable	Open	Pre-Closure	Closed	Spring	Neap
oWL	857	121	275	265	251
eWL	854	121	275	265	249
$u_{e2}$	686	119	254	203	203
$\rho_{e1}$	720	116	254	224	212
$\rho_{e2bot}$	354	84	219	102	104
$\rho_{e2top}$	203	60	160	46	72
$N_{e2}^2$	99	47	93	19	36
Dissolved oxygen <sub>e2bot</sub>	109	67	198	24	37
Dissolved oxygen <sub>e1</sub>	761	116	254	237	224
Turbidity <sub>e1</sub>	764	116	254	238	226
Waves <sub>ep</sub>	233	66	133	77	78

corroborated with time-lapse camera imagery). Pre-closure refers to 7 days prior to a mouth closure in order to capture the approach to closed conditions, when the estuary sill is often changing rapidly and the inlet is typically strongly constricted. For some analyses (as stated below), periods of high river flow (defined as any time 24 h before or after the stream gauge or the first EOF mode amplitude was in the top 5<sup>th</sup> percentile of measurements) were removed. Open period averages were further divided into spring and neap periods based on the top and bottom 33.3 percentiles of offshore tidal amplitude range ( $A$ ) (spring  $A > 1.78$  m; neap  $A < 1.35$ ).

**Fortnightly Phase Averaging** In a similar manner to the tidal phase averaging, variables were phase averaged over a spring-neap period. A spring-neap period is defined as half a lunar month (14.77 days). The start of each spring-neap period is defined as an offshore HHW event, and the end of the period is the nearest HHW event 14.77 days after the start of the spring such that  $\phi = 0$  and  $2\pi$  are the peak spring tide and  $\phi = \pi$  is the peak neap tide. Angle brackets with a  $\phi$  indicate spring-neap phase averaging,  $\langle \bullet \rangle_\phi$ . An individual spring-neap cycle for a given variable was only included in the fortnightly phase average if data was available for more than 50% of that spring-neap cycle, resulting in 63 realizations for the ADCP data (less for the CTD which has more bad data).

### Exchange Velocity

A theoretical approximation of the gravitationally driven component of the exchange velocity (i.e., the exchange driven by baroclinic density gradients rather than barotropic) is scaled as:

$$u_E^{theory} \approx \frac{g \langle D^3 \rangle \langle \frac{\Delta \rho_x}{\Delta X} \rangle}{\rho_o \langle \nu_t \rangle} \quad (4)$$

where  $g$  is the gravitational acceleration,  $D$  is the time-varying water depth,  $\frac{\Delta \rho_x}{\Delta X}$  is the longitudinal density gradient,  $\nu_t$  is an effective eddy diffusivity as defined for estuaries dominated by a pressure-friction balance (MacCready and Geyer 2010), and the brackets represent subtidal filtering. To estimate a diffusive exchange flow magnitude based on this theory using our data, we use the following approximation of this equation:

$$u_E^{theory} \approx \frac{g \langle D^2 \rangle \langle \frac{\Delta \rho_x}{\Delta X} \rangle}{\rho_o \sqrt{C_D} \langle U_T \rangle} \approx \frac{g \langle D^2 \rangle \langle \rho_{e3mid} \rangle - \langle \rho_o \rangle}{\rho_o \sqrt{C_D} \langle U_T \rangle} \quad (5)$$

where the density gradient is estimated between  $\rho_{e3mid}$  and  $\rho_o$  (for which  $\Delta X = 2$  km) and  $\nu_t$  has been scaled as

$\nu_t \approx \sqrt{C_D} U_T d \approx \sqrt{C_D} \langle U_T \rangle \langle D \rangle$ , where  $C_D = 1.0 \times 10^{-3}$  is a coefficient of drag,  $U_T$  is the absolute value of the depth-averaged velocity ( $U_T = |[u]|$ ) at the ADCP, and  $d$  is a representative channel water depth.

In a full derivation of the exchange flow (rather than a scaling), the magnitude of the gravitational exchange velocity has the same functional dependence as Eq. 4; however, a factor of 1/48 appears. Moreover, the relationship between  $\nu_t$  and  $\sqrt{C_D} U_T$  requires a scaling that has been found to vary greatly depending upon background stratification conditions. For an unstratified boundary layer, the maximum mid-depth  $\nu_t \approx 0.1 \sqrt{C_D} U_T d$  (e.g., Nezu and Rodi, 1986; Geyer and MacCready 2014); whereas for a stratified boundary layer,  $\nu_t$  is significantly reduced. Ralston et al. (2008) and MacCready (2007) scale the maximum  $\nu_t$  under stratification as  $\nu_t \approx 0.03 C_D U_T d$  which using  $C_D = 1.0 \times 10^{-3}$  is equivalent to  $\nu_t \approx 9.5 \times 10^{-4} \sqrt{C_D} U_T d$ , a factor of 100 smaller than the unstratified value, becoming even smaller when the bottom boundary layer takes up only a portion of the water column. Thus, the magnitude of the exchange flow estimate is ultimately very sensitive to the  $\nu_t$  parameterization.

The observed exchange flow throughout depth and time is defined as the subtidal velocities minus the 1st EOF mode such that  $u_E^{obs}(t, \sigma) = \langle u \rangle - EOF1$ . EOF1 is subtracted to remove the barotropic river flow, such that here our observed exchange flow is that due to baroclinic and intratidal processes and can be directly compared to Eq. 5. While this EOF decomposition is a mathematical tool, it often correlates with physical mechanisms. The dominant EOF mode is commonly related to the barotropic component of the flow and has been removed to isolate the subtidal sheared (baroclinic) estuarine circulation (e.g., Stacey et al. 2001; Giddings et al. 2014) as elaborated in the “Velocity EOFs” section and the Appendix. The time-varying magnitude of the exchange flow is defined as  $U_E^{obs}(t) = u_E^{obs}(t, \sigma_{max}) - u_E^{obs}(t, \sigma_{min})$ , where  $\sigma_{max}$  and  $\sigma_{min}$  indicate the vertical location of the maximum and minimum exchange flow in depth-normalized coordinates. If  $\sigma_{max}$  or  $\sigma_{min}$  are above or below the extrapolated locations, the last measured bin was used. The sign of  $U_E^{obs}$  is negative if the outflow is below the inflow (i.e., inverse estuarine exchange flow).

## Results

### Velocity EOFs

The first 3 EOF modes of the 1-h interpolated subtidal velocities for all available data explain 94.0%, 5.1%, and 0.01% of the variance, respectively. The first mode is unidirectional and correlates with river flow with the maximum correlation occurring when EOF mode 1 is

lagged 7 h behind the river flow ( $r=0.68, p < 0.001$ ). The 2nd mode has a single zero-crossing, consistent with a baroclinic vertical structure and correlates well ( $r=0.89, p < 0.001$ ) with the difference between  $\langle u \rangle$  at  $\sigma = 0.8$  and  $\sigma = 0.25$ . The second mode is positive (indicating velocities are out at the surface, in at depth, i.e., a classical estuarine circulation) 91.7% of the time when the estuary is open. The 2nd mode also correlates well with the observed exchange flow magnitude,  $U_E^{obs}$  ( $r=0.91, p < 0.001$ ) as expected because  $U_E^{obs}$  includes EOF modes 2 and higher, where EOF mode 2 represents a significantly larger velocity variance than any higher modes. The EOF vertical profiles and amplitude time series are shown in Appendix Fig. 11 and full re-constructed EOF mode 1–3 vertical velocities are shown in Appendix Fig. 12.

### Wave Field Offshore and in the Estuary

Wave energy was measured at 4 locations from offshore to upstream during each winter as described in the methods: oADV, szP, eP, and e2. The peak period of the offshore energy varies with longer period waves (shorter frequency) arriving before shorter period waves (higher frequency) (Fig. 3c). Note that while Fig. 3 shows data from winter 2017 (the period outlined by the second black rectangle on Fig. 2), the temporal and offshore to onshore trends are consistent year to year and Figs. 4 and 5 utilize all winter data (orange lines on Fig. 2). Most of the offshore energy was in the swell band (Figs. 3c and 4). Moving inshore to the surfzone, szP, there is less total energy and the peak period has increased (Fig. 3d). At szP, the height of the swell waves is much smaller than offshore, but the height

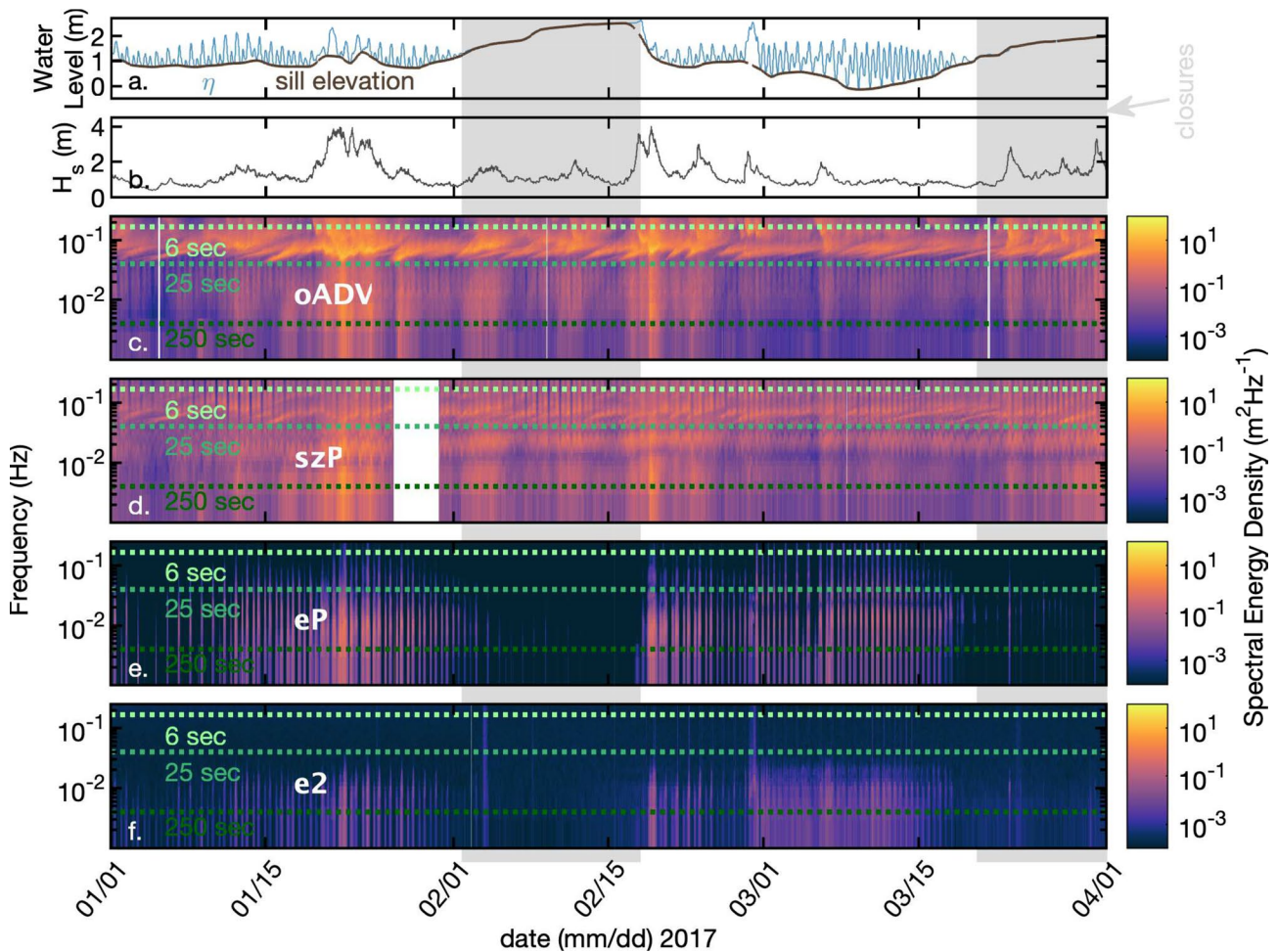


**Fig. 3** Wave energy along estuary. A 3-month time series of **a** water level (blue), sill elevation (brown), **b** offshore significant wave height (CDIP Buoy #100), and **c–f** wave energy spectrograms (in 30-min segments) progressing from offshore (**c**, oADV), to the surfzone (**d**, szP), into the estuary inlet (**e**, eP), and upstream (**f**, e2). Horizontal green lines indicate periods of 6 s (light green), 25 s (medium green),

and 250 s (dark green) for reference. Yellow indicates more energy while dark purple indicates less. Note that the colorbar on **c–f** are the same; however, **f** is beginning to hit the instrument noise floor. Gray bars across all panels indicate two periods of closure within this 3-month time series

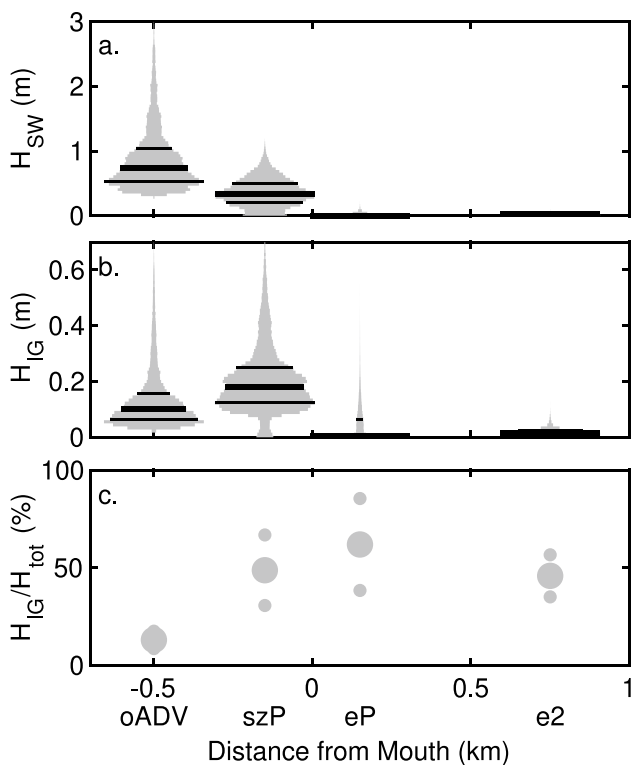


**Fig. 4** Wave data summary. Significant wave height violin plots of swell **a** and IG **b** energy bands measured in 8 m of water (oADV, 0.5 km offshore), the surfzone (szP, 0.15 km offshore), inside the estuary inlet (eP, 0.15 km upstream), and upstream (e2, 0.75 km upstream). The violin plots show the full histogram in gray with black lines marking the 25th, 50th (thick), and 75th percentiles. Note that oADV  $H_{SW}$  and  $H_{IG}$  and szP  $H_{IG}$  contain a few values beyond the axes upper limits (up to 3.9 for  $H_{SW}$  and 1.1 for  $H_{IG}$ ), but represent such a small fraction of the total data that the histogram becomes essentially invisible. **c** Percent of IG significant wave height vs total spectrum wave height. The large dots are the mean, the smaller dots indicate  $\pm$  one standard deviation. The ADCP pressure sensor error was larger and the sampling interval longer which may have artificially increased the amount of total wave energy resulting in a lower  $H_{IG}/H_{tot}$  value

of the IG waves is larger than offshore (and the largest of the four locations) (Fig. 4b). Moving upstream, the total amount of energy decreases with very little wave energy when the estuary is closed (Fig. 3). When the waves offshore are large (Fig. 3b) and the sill is low (Fig. 3a), IG waves are able to make it up to e2, 0.75-km upstream (Fig. 3f). The highest percentage of total energy in the IG band is found inside the estuary mouth, at eP (Figs. 3e and 4c). The IG percent of total energy at e2 is also high but slightly smaller, potentially because of the higher noise floor of the instrumentation.

In the inlet, the total amount of wave energy is dependent on the offshore wave height (Fig. 3), the tidal current velocity, and the offshore water level relative to the sill height (Fig. 5). The ratio between the IG wave energy at eP and that at szP (i.e., the fraction of IG energy in the surfzone that

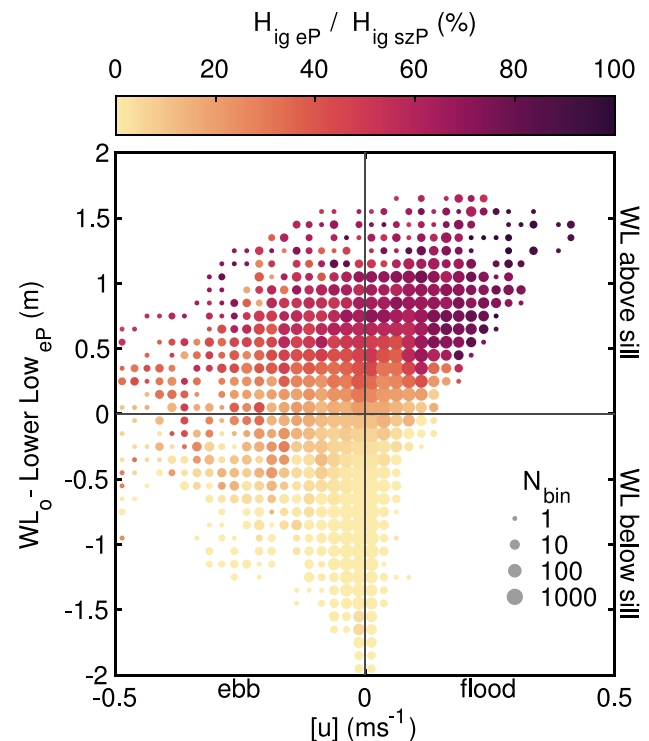


**Fig. 5** IG wave height reduction in inlet. All available open period data in a 2-D histogram of the water level height above the sill (water level offshore minus the lower-lower water level at eP such that values  $> 0$  indicate the offshore water level is above the sill) against depth-averaged currents at e2 (where  $[u]>0$  indicates a flood tide) where the size of the dot indicates the number of samples in each bin. The dot is colored by the average wave height reduction for all data that is in each bin. The wave height reduction is defined as the percent of wave height inside the estuary inlet, eP, relative to the surfzone, szP (i.e., 100% times  $H_{IG}$  at eP divided by  $H_{IG}$  at szP) where the lightest yellow indicates that surfzone waves do not reach the inlet sensor and dark pink indicates that waves at eP are the same size as those in the surfzone. The estuary IG wave height is greatest compared to that in the surfzone (dark pink) when the offshore water level is high compared to the sill height and during strong flooding tides (upper-right quadrant)

propagates into the estuary) is near zero (light yellow, Fig. 5) when the offshore water level is lower than the sill height. The fraction of surfzone IG wave energy that makes it inside the estuary is largest (dark pink, Fig. 5) when velocities at e2 are flowing into the estuary ( $[u] > 0$ , flooding current) and when the offshore water level is high relative to the sill height (upper-right quadrant of Fig. 5). Wave-current interaction can impede or facilitate wave energy propagation through the inlet to up-estuary locations. At the same relative water levels, less IG wave energy is able to propagate upstream during ebb tides, while during flood tides, IG wave energy can propagate upstream with minimal dissipation (Fig. 5).

The short-term eADV deployment exemplifies this wave-current interaction and the impact on suspended sediment

(Fig. 6). As the magnitude of outflowing velocity decreases at eADV (Fig. 6a) and the water levels start to increase within the estuary (Fig. 6b), some small waves reach the sensor at eP (Fig. 6c, grey). When the velocity switches sign to a flooding current at eADV (Fig. 6a, red fill), the waves are able to propagate further (Fig. 6c, black). The waves reach the furthest distance upstream (e2, Fig. 6c, blue) during inflowing velocities when the tide is highest (Fig. 6b). Note that there is a ~35 min lag between the start of the flood tides and the waves reaching eADV during the first larger flood tide. When wave fluctuations are present at eADV the optical backscatter, a proxy for suspended sediment concentrations increases substantially. The OBS voltage decreases over the course of the flood tide, which may suggest that the bottom stress influencing sediment resuspension is related to the ratio of the wave height to the total water depth, i.e., the bottom-orbital velocity magnitude over the flood tide likely decreases as water levels increase. The presence or absence of waves relative to the water level and velocity shown in Figs. 5 and 6 highlights the importance of both waves and currents impacting wave propagation. Carefully examining Fig. 6, the same water level during flood shows a backscatter signal while during ebb it does not, consistent with the larger wave signal during the flood. Similarly at the same mean current magnitude, backscatter is highest again during the flood when waves are larger. Overall, Fig. 6 shows that high

backscatter is only present when the waves are present, thus suggesting a link between waves and currents on sediment transport.

### Semidiurnal (2xM<sub>2</sub>) Circulation during Open, Pre-closure, and Closed Periods

To explicitly examine the mixed semidiurnal tide with the larger and smaller tides, a phase average (see the “Tidal Phase Averaging” section) of a lunar day or  $2 \times M_2$  is examined. Hereafter, the larger tide will refer to the  $M_2$  tide with the higher depth-averaged velocities ( $\sim 0$  to  $\sim \pi$ , Fig. 7f) and the smaller tide will refer to tide with the lower depth-averaged velocities ( $\sim \pi$  to  $\sim 2\pi$ , Fig. 7f).  $\pi/2$  and  $3\pi/2$  approximately denote transitions from flood to ebb within the larger and smaller tides respectively. These transitions are approximate as the flood and ebb tides are not symmetric. This will be done for different estuary conditions including open, pre-closure, and closed periods (below) and spring, neap periods (the “Circulation during Spring and Neap Periods” section). As a reminder, the number of individual tidal cycles that go into these phase averages is shown in Table 1. Because these are phase averages over many tidal cycles, individual tidal cycles differ from these average pictures and this variation is discussed briefly following the “Semidiurnal (2xM<sub>2</sub>) Phase Averages During Spring and Neap Periods” section.

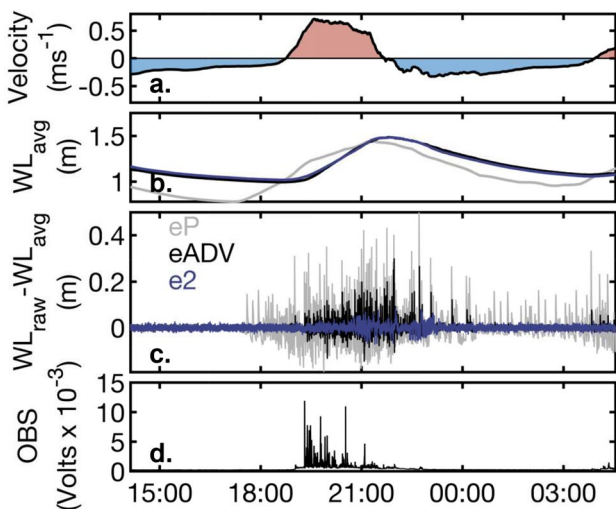


**Fig. 6** Snapshot of wave-current interactions. **a** 30-min average velocity data at ADV ~.4 km upstream (eADV). Blue (red) fill indicates outflowing (inflowing) velocity at eADV. **b** 30-min averaged water level at eP (gray), eADV (black), and e2 (blue). **c** Raw water level minus 30-min averaged water level at eP, eADV, and e2. eP sampled at 2 Hz; eADV sampled at 8 Hz; e2 sampled at 0.5 Hz. **d** Turbidity from optical back scatter sensor in un-calibrated voltage. Because this sensor is un-calibrated, results are to be interpreted qualitatively. Deployment occurred during the low tide through the lower high and subsequent low. The sill was about 1.01 m high during this deployment

#### Open

During open periods, the phase-averaged offshore tide,  $\langle \eta_o \rangle_\tau$ , has a range of 1.54 m between HHW and LLW while the phase-averaged estuarine water level,  $\langle \eta_e \rangle_\tau$ , has a range of 0.75 m (Fig. 7a.i). The HHW in the estuary is lagged 0.66 h behind the tide offshore (measured 7.5 km from the mouth) while the LLW in the estuary is lagged 2.32 h behind the LLW offshore. The normalized skewness of the water level rate of change is negative offshore, while it is positive in the estuary ( $\gamma_0^{o, \langle \delta \eta / \delta t \rangle_\tau} = -0.15$ ;  $\gamma_0^{e, \langle \delta \eta / \delta t \rangle_\tau} = 0.60$ ), indicating that the duration of the falling tide in the estuary is longer than the rising tide and is significantly different from the nearly symmetrical offshore water level (Nidzicko and Ralston 2012).

Near-bottom estuarine density,  $\langle \rho_{e2,bot} \rangle_\tau$ , is slightly less dense than offshore,  $\langle \rho_o \rangle_\tau$  (Fig. 7b.i.). Near-surface estuarine density,  $\langle \rho_{e2,top} \rangle_\tau$ , is the least dense near the end of the smaller ebb tide, just before the start of the larger flood tide, and densest at the end of the larger flood tide. This results in maximum bulk stratification ( $N^2 = 0.034 \text{ s}^{-2}$ ) near the end of the smaller ebb tide and minimum bulk stratification ( $N^2 = 0.010 \text{ s}^{-2}$ ) near the end of the larger flood (Fig. 7b.i.).  $\langle DO_{e2,bot} \rangle_\tau$  generally has similar dissolved oxygen concentrations to  $\langle DO_{e1,mid} \rangle_\tau$ . However,

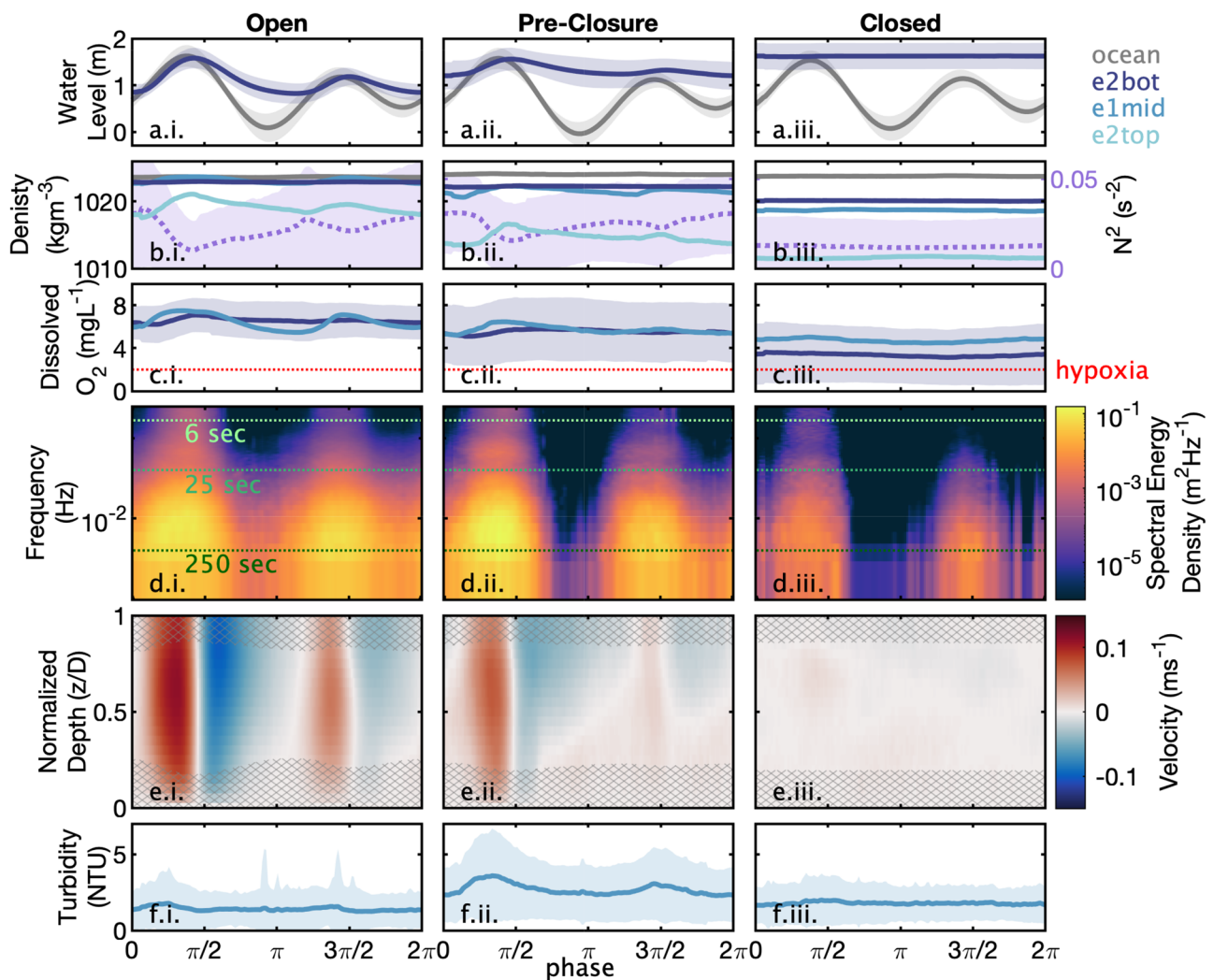


**Fig. 7** Tidal phase averages ( $2xM_2$ ) for open periods (i.), pre-closure periods (ii.), (defined as one week before closure), and closed periods (iii.). 0 and  $2\pi$  correspond to the estuary slack currents preceding the offshore higher-high water level. **a** Water level offshore (gray) and in the estuary (blue) in NAVD88. **b** Density offshore (gray), at e2bot (dark blue), e1mid (medium blue), and e2top (light blue). Stratification (purple, dashed) based on e2bot and e2top density and water depth (note: number of samples for e2top density and stratification are reduced.). **c** Dissolved oxygen at e2bot (dark blue) and e1mid (medium blue) where a red dotted line indicates hypoxia. **d** Wave energy at eP, where yellow indicates more energy on a logarithmic

colorbar. Horizontal green lines indicate periods of 6 s (light green), 25 s (medium green), and 250 s (dark green). **e** Along-stream velocity at e2 in depth-normalized coordinates where red indicates positive velocities into the estuary (i.e., flooding), blue indicates negative velocities out of the estuary (i.e., ebbing). Gray hatching on **e** indicates the phase-averaged region of extrapolated data. **f** Turbidity (in NTU) at e1mid from the lab-calibrated, integrated EXO turbidity sensor. Prior to phase averaging, the turbidity spikes  $>100$  NTU were removed. Shading on **a**, **b** ( $N^2$  only), **c**, and **f** indicates  $\pm$  one standard deviation of the phase average

$\langle DO_{e1, mid} \rangle_\tau$  is more variable throughout the tidal cycle (Fig. 7c.i.), potentially due to both its height in the water column and location closer to the estuary mouth.

Depth, phase-averaged velocity,  $\langle [u] \rangle_\tau$ , ranges from  $-0.07$  to  $0.09$   $m\ s^{-1}$ . The ebb tide velocity is weaker, and the ebb is longer in duration ( $\langle [u] \rangle_\tau$  is in the ebb direction 57% of the time). The normalized skewness of the velocity ( $\gamma_0^{e, \langle [u] \rangle_\tau} = 0.66$ ) indicates flood dominance. The maximum velocity during the flood tide is at mid-depth ( $\sigma=0.65$ ) while

the maximum velocity during the ebb tide is closer to the surface ( $\sigma=0.85$ ) (Fig. 7e.i.). The velocity is relatively more depth-uniform during flood tides with higher mid-water column shear during ebb tides. Note that hatched areas in Fig. 7e indicate the phase-averaged location of extrapolated data.

As shown with the analyses described in the “Wave Field Offshore and in the Estuary” section, tidal phase averages confirm that wave energy just inside the inlet (measured at

eP) is dependent on the tidal amplitude as well as the magnitude and direction of velocity. Wave energy is larger during flooding tides and when the offshore water level is higher (Figs. 3, 5, 7d.i.). During the larger flooding tide and into the maximum high tide, the wave energy is greatest with the highest frequency of waves able to propagate into the mouth. Wave energy is lowest (and in lower frequencies) during the latter part of the larger ebb when the velocities are out of the estuary and the water level offshore is low.

The turbidity generally increases slightly during the flood tides (Fig. 7d.i.) and correlates with the depth-averaged velocity ( $r=0.73$ ,  $p=0.002$ ). However, the turbidity signal is variable with the standard deviation over 2.8 times the range of the phase-averaged turbidity signal.

### Pre-closure

During pre-closure periods (defined as 7 days before a closure),  $\langle \eta_e \rangle_\tau$  decreases to 0.36 m between HHW and LLW while the asymmetry increases,  $\gamma_0^{e, \langle \delta \eta / \delta t \rangle_\tau} = 1.01$  (Fig. 7a.ii.). The surface water density is generally fresher and fluctuates less throughout a tidal cycle than during the open period; however, the bottom water also freshens, resulting in only slightly higher stratification. The lowest stratification still occurs near HHW and the highest stratification remains at the end of the smaller ebb/start of the large flood tide (Fig. 7b.ii.). DO is slightly lower and the mid-water column DO varies less compared to open periods.

The maximum value of  $\langle [u] \rangle_\tau$  has decreased to  $0.06 \text{ m s}^{-1}$  during the flood and  $-0.03 \text{ m s}^{-1}$  during the ebb tide. The normalized velocity skewness indicates even stronger flood dominance than during the open state ( $\gamma_0^{e, \langle [u] \rangle_\tau} = 1.64$ ). During the pre-closure period, nearly the entire ebb is constrained above the mid-water column depth while the bottom water is moving in the upstream direction (Fig. 7e.ii.) leading to increased mid-water column shear during the ebbs.

During the pre-closure period, the maximum phase-averaged IG wave height,  $\langle H_{IG} \rangle_\tau$ , is 2.3 times higher than during the open period. There is very little wave energy during the ebbing tide (Fig. 7d.ii) near offshore low water levels because the combined wave swash elevation and offshore water level are not large enough to reach above the sill height (Fig. 7a.ii.). Despite reduced upstream currents, the turbidity is higher than during the open period, particularly during flood tide periods with large wave energy. The increase in turbidity for the pre-closure period is associated with typically larger waves that precede closure, as discussed further in the “Waves” section. Note that the choice of 7 days pre-closure, rather than a sill height cutoff, was chosen to elucidate factors occurring in the approach to closure, not just constricted conditions.

### Closed

During closed periods,  $\langle \eta_e \rangle_\tau$  does not vary with the offshore tidal phase and is consistently elevated above  $\langle \eta_o \rangle_\tau$ . The densities at all estuary locations are fresher and the DO is lower than during either pre-closure or open periods. Velocities are very small ( $\langle [u] \rangle_\tau < 0.004 \text{ m s}^{-1}$ ). During the closed phase, waves occasionally overtop the sill during offshore high tides resulting in some wave energy propagating into the inlet. The wave energy able to make it over the sill is primarily in the IG band with more energy able to propagate in during higher offshore water levels.

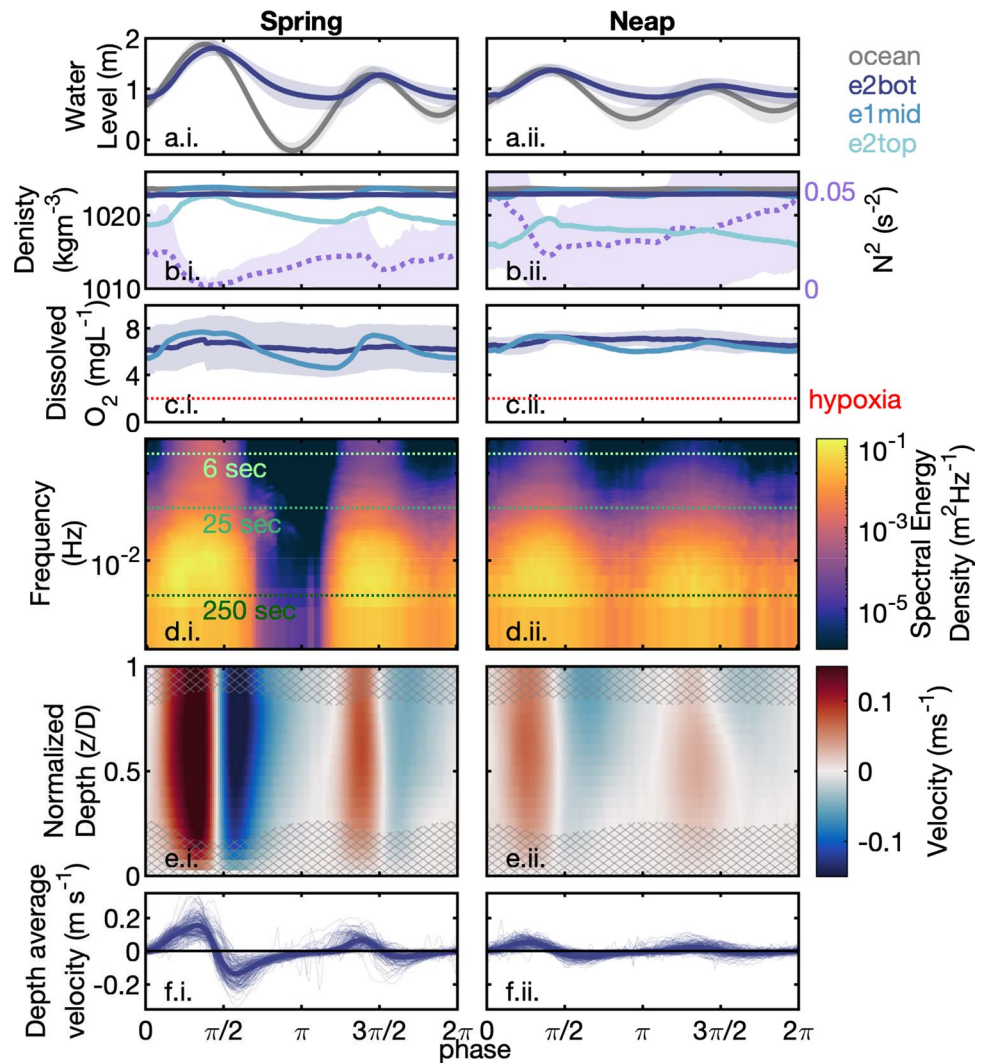
### Circulation During Spring and Neap Periods

#### Semidiurnal (2xM<sub>2</sub>) Phase Averages During Spring and Neap Periods

During spring tides,  $\langle \eta_e \rangle_\tau$  has a larger maximum tidal range than during neap tides (0.97 m and 0.52 m between HHW and LLW, for spring and neap tides respectively) (Fig. 8a), directly related to the method by which spring and neap tides are defined as explained in the “Tidal Phase Averaging” section). The skewness of the water level rate of change is similar between the spring and neap tides both within the estuary ( $\gamma_0^{e, \langle \delta \eta / \delta t \rangle_\tau} = 0.65$  and  $0.57$ ) as well as offshore, ( $\gamma_0^{o, \langle \delta \eta / \delta t \rangle_\tau} = -0.19$  and  $-0.05$  for spring and neap, respectively). The velocity skewness, however, is much larger during neap tides ( $\gamma_0^{e, \langle [u] \rangle_\tau} = 0.41$  and  $1.20$ , for spring and neap, respectively).  $\langle [u] \rangle_\tau$  during spring tides is much larger ( $\sim 3$  times) than during neap tides (Fig. 8f). Velocities extend deeper into the water column during spring tides (Fig. 8e). DO in the mid-water column is more variable during Spring tides (Fig. 8c) and turbidity is slightly higher (not shown). Wave energy is largest during the large spring flood tide and lowest during the lowest spring tide water levels (Fig. 8d).

While we focus on leveraging our long time series to illustrate tidal averages (Figs. 7 and 8), it is worth briefly noting that deviations from these averages occur over individual tidal cycles, which show variability relative to the mean largely due to the tidal range, and to a smaller degree due to individual differences over time (i.e., wind, precipitation, sill height). For example, peak currents during spring, open tides (Fig. 8e.i.) can vary from  $0.12$  to  $0.45 \text{ m s}^{-1}$  (with a median of  $0.21 \text{ m s}^{-1}$ ). Figure 8f.i, f.ii. demonstrates the variability in individual tidal cycle  $[u]$ . Moreover, we focus on density (Figs. 7b and 8b) since ultimately it is variations in density that drive baroclinic pressure gradients. Salinity in the estuary ranges from nearly 0 (1.1, measured at the surface during a neap tide) to slightly hypersaline (34.6, measured near the bed during a neap tide). Temperature varies from  $6.2$  to  $29.2 \text{ }^\circ\text{C}$  near the surface with less variation at depth where the diurnal

**Fig. 8** Tidal phase averages ( $2 \times M_2$ ) for spring (i.) and neap (ii.) periods. Same as Fig. 7 but split into spring and neap periods based on the water level range as described in the “Tidal Phase Averaging” section. Note that panel f is different from Fig. 7f. f here shows phase-averaged depth-average velocity ( $\langle u \rangle$ , thick blue line) with all individual tidal cycles going into that phase average shown in very thin blue lines



cycle is muted ( $13.3\text{--}27.7\text{ }^{\circ}\text{C}$ ). As is discussed further below, the density in the main arm of this estuary remains salinity dominated throughout the year with salinity explaining 98% of the density variance on average. The smaller estuary side arm (Fig. 1, stations TJSW and TJSE), with a smaller watershed, does become hypersaline during the summer months.

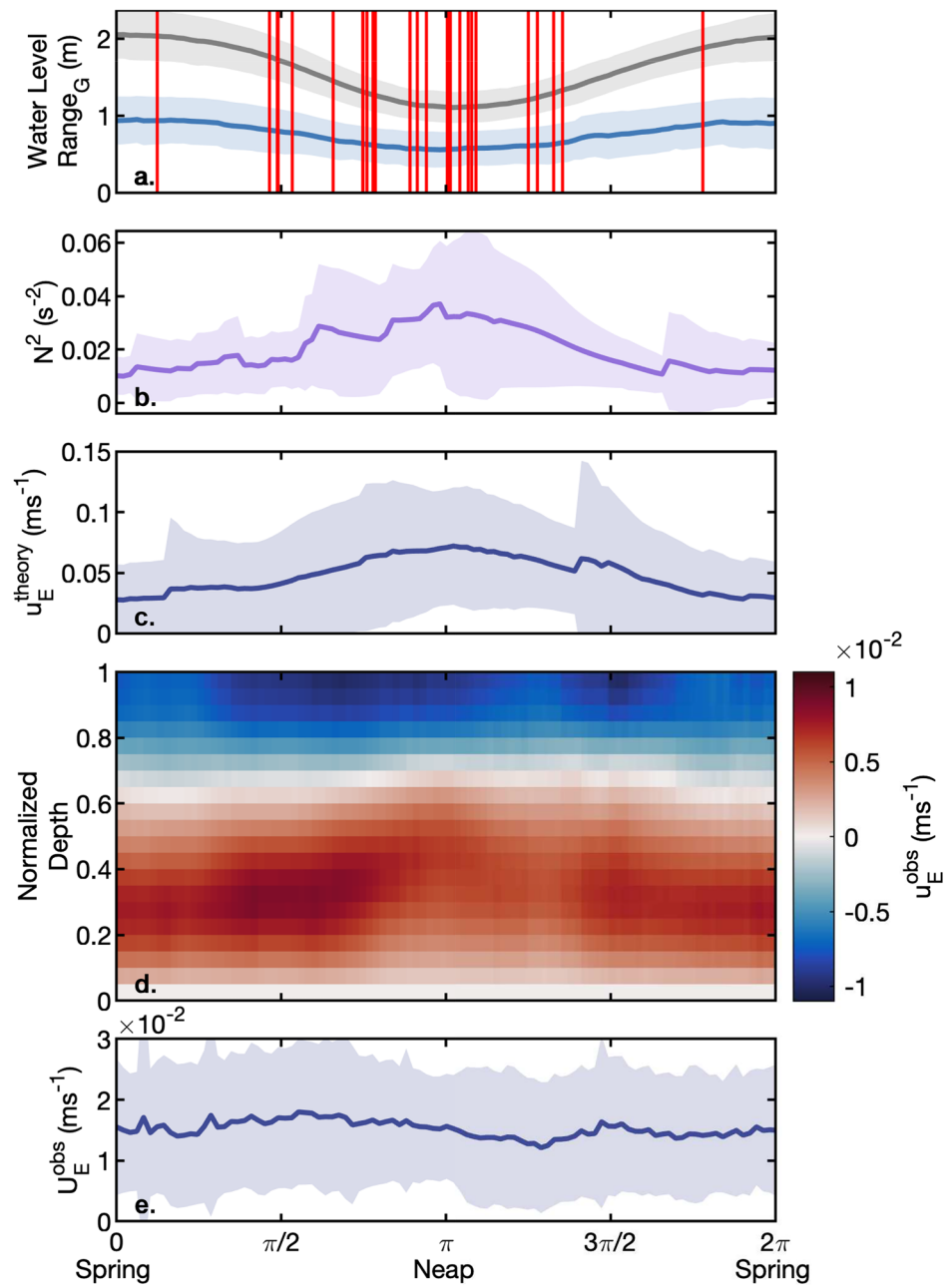
### Fortnightly Phase Averages

When the subtidal data is phase averaged based on a fortnightly or spring-neap cycle (the “Fortnightly Phase Averaging” section) during the open, low river flow periods, the estuary water level range (HHW minus LLW) exhibits a smaller variation than the offshore range Fig. 9a). The  $\langle h_{sill} \rangle_{\phi}$  does not exhibit a clear spring-neap cycle and has a very large standard deviation (not shown). Nonetheless, the majority of the mouth closures (red lines, Fig. 9a), 75%, occur during the neap tide compared to only 7% during the spring tide (defined as the bottom and top 33.3 percentile of offshore tidal amplitude range respectively;

even more, 82% of closures occur during neap if defined as between  $\pi/2$  and  $3\pi/2$  fortnightly phase). The vertical stratification,  $\langle N^2 \rangle_{\phi}$ , (Fig. 9b) and the along-channel density gradient,  $\langle \frac{(\rho_{e3}) - (\rho_o)}{\Delta X} \rangle_{\phi}$  (the latter not shown), are maximums during neap tides. The theoretical estuarine exchange flow estimated using in situ variables,  $\langle u_E^{theory} \rangle_{\phi}$ , (Eq. 5, Fig. 9c) is a maximum during neap tide and a minimum during spring tide. However, the observed exchange flow  $\langle u_E^{obs} \rangle_{\phi}$  (and  $\langle U_E^{obs} \rangle_{\phi}$ ) for the entire open time period (except during extreme river flows) is a maximum at the end of the spring tide (Fig. 9d–e) with a weak fortnightly signal.

To try to understand the unexpected temporal variability in  $u_E^{obs}$  and  $U_E^{obs}$ , we further separate the exchange flow calculations based on the sill height in order to compare more open and more constricted conditions. When the exchange is calculated only during the lowest sill elevations (sill below 0.69 m, NAVD88, lowest 1/3 of sill height measurements), and also restricting to open, non-extreme river flows, the

**Fig. 9** Spring/neap cycle: Phase averages over the spring-neap cycle (14.77 days) where 0 and  $2\pi$  are peak spring tides, and  $\pi$  is a neap tide. **a** Water level range for offshore (gray) and estuary (blue). Shading indicates  $\pm$  one standard deviation. Red lines mark the starting phase for all closures. **b** Stratification (purple) based on bottom (e2bot) and surface density (e2top) and water depth. **c** Theoretical exchange velocity estimated using Eq. 5. **d** Observed exchange velocity (defined as the subtidal velocity minus the EOF mode 1 velocity,  $u_E^{obs}(t, \sigma) = \langle u \rangle - EOF1$ ) phase-averaged in depth-normalized coordinates. **e** Strength of the exchange velocity,  $U_E^{obs}(t)$  as explained in the “Exchange Velocity” section. The number of realizations varies depending upon the data quality with 74, 9, 43, 62, and 62 realizations averaged into **a–e** respectively. Note that each realization does not always cover a full spring/neap cycle resulting in occasional jumps in the averages and/or standard deviations



exchange flow strength is a minimum during spring, increasing to a maximum during the neap tides (Fig. 10, dashed lines). When the sill was high (above 0.89 m, NAVD88, highest 1/3 of sill height measurements), the exchange strength was greatest during spring and between spring and neap and lowest during the neap tide.

**Discussion**

The objective of this paper is to understand how the dynamics of a small, shallow, bar-built, intermittently closed estuary change over various time scales (including

tidal, diurnal, spring-neap, seasonal, and interannual), morphological conditions, and place the results in the context of estuarine theory.

**Estuarine Response to Interannual Variability of Atmospheric and Wave Forcing**

Over the period of data collection, December 2014–June 2019, several distinct large-scale oceanic and atmospheric forcing events occurred including a marine heatwave (“The Blob”), a large El Niño, and anomalously wet and dry years. This interannual variability impacted both upstream (with fluctuating river flows) and downstream of the estuary (with

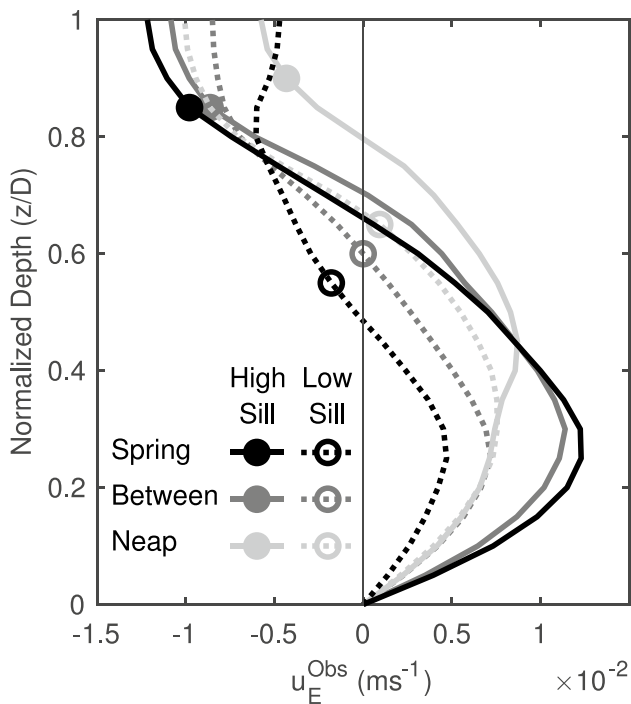


**Fig. 10** Mean exchange velocity profiles for low sill elevation (dashed lines, open circles) and high sill elevation (solid lines, solid circles) for spring tides (black), between spring and neap period (dark gray), and neap tides (light gray). The circles indicate the mean sill height over each averaging period

varying wave conditions and offshore water levels). River discharge can affect the degree of stratification and strength of the tidal and residual circulation in the estuary directly (e.g., Hansen and Rattray 1966; Geyer and MacCready 2014). Both the amount of river flow and the offshore water levels and wave energy affect the sill height (Behrens et al. 2013; Rich and Keller 2013), which in turn impacts the circulation, sediment transport, and mixing near the inlet (Largier et al. 1992; Gale et al. 2007; Cousins et al. 2010; Behrens et al. 2016).

The 2014–2015 Blob resulted in small waves, high air and sea surface temperatures, high atmospheric pressure (Bond et al. 2015; Hartmann 2015), and small river flows (Fig. 2f). During the summer and early fall, weak and sometimes negative exchange occurred (negative exchange 32.6% of the time from 01 June 2015 to 30 September 2015, Fig. 2b), hypothesized due to weaker along-stream density gradients. The side estuary arm that has a smaller watershed went hypersaline during these periods as evidenced from comparing the salinity at TJSW to offshore salinity (not shown).

The 2015–2016 El Niño brought extremely large waves and below average precipitation (Ludka et al. 2016; Barnard et al. 2017; Siler et al. 2017; Young et al. 2018). The large waves and lack of river flows (Fig. 2f) during the El Niño caused significant accretion to estuarine inlets all along

the Southern California Bight (Young et al. 2018; Harvey et al. 2020) and increased estuarine inundation (Goodman et al. 2018; Harvey et al. 2020). In LPL, the anomalously strong wave conditions and weak precipitation (thus small river flow) contributed to 2016 having a total of 235 closed days, far exceeding the annual average (excluding 2016) of 42 closed days since 2004. The significant increase in closed conditions is readily apparent by the gray bars on Fig. 2.

The 2016–2017 winter was an anomalously wet winter (precipitation at San Diego Airport was 41% above the 1939–2019 winter average) with large river flows and large waves (Fig. 2f). The largest river flow event of the study period occurred in the last week of February 2017 which resulted in extremely high velocities ( $[u] = 2.00 \text{ m s}^{-1}$ ) at e2. The large velocities scoured the sill to the lowest sill elevation for the study period ( $\sim -0.1 \text{ m NAVD88}$ ), which persisted through summer and fall 2017 along with more symmetric water levels and velocities (Fig. 2a, c).

The 2017–2018 winter was extremely dry with low river flow and small waves (winter precipitation at San Diego Airport was in the bottom 5 percentile, 61% below 1939–2019 winter average). Sill elevations during spring 2018 were fairly high resulting in higher water level and velocity asymmetry (Fig. 2c). The 2018–2019 winter had moderate waves and high precipitation (precipitation at San Diego Airport 37% above 1939–2019 average) and river flows. The sill was scoured to its second lowest level during the study period in February 2019 (Fig. 2a).

The interannual variability in oceanic and atmospheric forcing results in changes to the sill height where waves generally accrete the sill and precipitation (i.e., river flows) erodes the sill as elaborated upon below. The sill height in turn affects the tidal circulation, residual circulation, and the amount of wave energy in the system.

## Drivers of Inlet Accretion and Erosion

### River Discharge

River discharge is one of the main drivers of inlet erosion (Ranasinghe et al. 1999; Behrens et al. 2013; Rich and Keller 2013). As described above, following large discharge events, the sill was generally low (Fig. 2a, f) with the lowest sill observed after the largest river discharge event. During particularly dry periods the sill steadily grew (i.e., 2017–2018).

### Tidal Asymmetry

Despite asymmetry (Eq. 2) indicating an ebb-dominant tide offshore (Nidzicko 2010) (average  $\gamma_0^{e,\delta\eta/\delta t} = -0.13$  during the study period), the asymmetry for both water level and tidal velocities within the estuary are indicative of a flood-dominant estuary (average  $\gamma_0^{e,\delta\eta/\delta t} = 0.99$ ;  $\gamma_0^{e,u} = 0.76$  during

the study period) and thus the bed-load sediment transport of coarse sediments is directed into the inlet (Dronkers 1986). Additionally, the mouth geometry (Eq. 3) is positive ( $\gamma_{inlet} = 0.72$ ), also indicative of a flood-dominant inlet (Friedrichs and Madsen 1992; Nidzicko 2010). Over a phase-averaged tidal period, velocity asymmetry in the estuary,  $\gamma_0^{e,(in)}\tau$ , becomes much more positive during the neap periods. As the velocity is responsible for sediment movement, the more positive (flood-dominant) skewness is likely a contributing factor to the fact that closures are more common during neap tide (Fig. 9a). There is also a potential feedback loop in sediment transport and accretion because as the sill grew over the course of the winter/early spring each year, the tidal asymmetry also increased (Fig. 2a, c).

## Waves

During the study period, the largest offshore waves occurred during the 2015–2016 El Niño winter (Ludka et al. 2016; Barnard et al. 2017; Young et al. 2018). As estuary and surf-zone wave measurements were only taken during the winter months (Fig. 3), the estuary and surfzone wave energy in Fig. 4 represents periods of only larger winter offshore waves. The sill is generally higher during the winter months partially due to wave build up, and partially due to timing of dredging (which typically occurs during the spring).

Wave energy in the estuary is dependent on the magnitude and direction of velocity at the inlet, the offshore water level relative to the sill height (Figs. 5 and 6), and the amount of offshore wave energy (Fig. 3a) (Bertin and Olabarrieta 2016; Williams and Stacey 2016; Bertin et al. 2019). IG waves can only propagate into the estuary when the offshore water level relative to the sill height is greater than zero with more IG waves (darker colors, Fig. 5) propagating into the system as the relative water level increases. When comparing similar water levels, the largest IG waves propagate into the estuary during fast flooding currents due to wave-current interactions, while waves are blocked from entering the inlet by ebbing currents (Figs. 5 and 7d.i) (similar to Bertin and Olabarrieta 2016; Williams and Stacey 2016; Bertin et al. 2019).

The largest  $H_{IG}$  values seen in the estuary are during strong flood tides (Figs. 5 and 7d) and periods of high offshore waves (Fig. 3).  $\langle H_{IG} \rangle_\tau$  waves in the inlet are ~1.5 times greater during the larger spring flood tides than during the larger neap flood tides (Fig. 8e). During large spring ebb tides,  $\langle H_{IG} \rangle_\tau$  is near zero while some energy is able to enter the system during the neap ebbs (Fig. 8e). (Note: during several particularly large tidal cycles of the 2017–2018 winter there were symmetric sinusoidal waves at eP during the large ebb tide potentially due to strong currents creating a wake from the pressure sensor pole. This resulted in a peak

in energy during the larger ebb tides between ~20 and ~35 s in Fig. 8d.i). Moving onshore and upstream, both IG and higher frequency waves dissipate (resulting in a decrease in total energy, Figs. 3 and 4). The percent of IG energy relative to the total wave energy within the estuary is higher compared with the surfzone and offshore because the sill acts as a low-pass filter (Fig. 4).

IG waves bring in beach sand due to a combination of bed-load and suspended sediment transport (Figs. 6d and 7f). During the flood tides, there is a stronger signal of turbidity (Figs. 7f.i, f.ii and 6d) consistent with both higher near-bed velocities, higher near-bed shear, and larger waves (similar to Bertin et al. 2019). The maximum  $\langle H_{IG} \rangle_\tau$  was observed during the pre-closure period during the large, flooding tide (~1.8 times the maximum  $\langle H_{IG} \rangle_\tau$  during spring tides and ~2.3 times all open tides). This high wave energy in the estuary during the 7 days preceding closure was due to high energy offshore. High turbidity (Fig. 7f.ii.) during these large wave events is indicative of high sediment transport that likely facilitated the closures.

In summary, similar to other studies (Ranasinghe et al. 1999; Behrens et al. 2013; Rich and Keller 2013), river discharge transports sand out of the LPL inlet while velocity asymmetry and the propagation of larger waves during flood tides drive sediment transport into the estuary. Despite the erosion caused by the river discharge, there is generally a net accretion in the inlet over the winter and early spring resulting in inlet closures nearly every year with earlier and more frequent closures during years with lower discharge and/or higher waves (Fig. 2a) (Hastings and Elwany 2012; Young et al. 2018). The sill accretion can have profound impacts on the tidal and estuarine circulation as described below.

## Tidal and Fortnightly Circulation

The estuary bottom water is generally slightly less dense than the water offshore (Fig. 7b.i.) indicating that the bottom water is subject to mixing within the estuary. Despite limited data availability, existing data suggests that the surface water was least dense near the end of the small ebb leading to maximum stratification at the end of the small ebb/start of the large flood as expected by strain-induced periodic stratification (SIPS, Simpson et al. 1990). Within the spring-neap cycle, the stratification was generally higher during the neap (Figs. 8b.i., b.ii. and 9b) than during the spring leading to the minimum stratification near the end of the stronger flood tides during spring and maximum stratification at the end of the weaker ebb tides during neap periods, as expected in a classical estuary (Geyer and MacCready 2014). As the estuary started to close, the estuary freshened and stratification slightly increased compared to during the fully open period (Figs. 7b.ii. and 2d).

The velocities are strongest and more depth-uniform during the flood (Fig. 7e.i.) leading to lower shear within the water column than during the ebb when the velocities are more surface intensified, also consistent with SIPS. The strongest shear within the water column occurs during the strong spring ebb tides (Fig. 8e.i.). During neap tides, the weaker flood tide is deeper in the water column resulting in higher mid-water column shear Fig. 8e.ii.), again consistent with classical circulation in larger estuaries (Geyer and MacCready 2014).

Overall, the variability of the circulation, tidal velocities, water depth, and stratification of LPL are strongly dependent on the sill height and episodic river flow. When the river flow and sill are low, the estuary responds similarly to classical estuaries exhibiting similar intratidal and spring/neap variations in stratification, shear, and mixing. Using the Geyer and MacCready (2014) freshwater Froude number ( $Fr_f = U_R / (\beta g s_{ocean} h)^{1/2}$  where  $U_R$  is the river flow,  $\beta$  is the haline contraction coefficient and  $s_{ocean}$  is the oceanic salinity) and mixing ( $M^2 = C_D U_T^2 / (\omega N_o h^2)$  where  $N_o = (\beta g s_{ocean} / h)^{1/2}$ ), parameterization, where the amount of mixing varies with the spring-neap cycle, water depth, stratification, and the sill height, and the estuary spans a wide parameter space including strongly stratified, partially mixed, and SIPS-type estuary. During periods of extremely high river flow (removed from the phase averages due to its episodic nature, described more below), the freshwater Froude number can increase considerably causing the system to behave more like a tidal salt wedge (Geyer and MacCready 2014) where the salinity is expelled every tidal cycle (e.g., Ralston et al. 2010; Giddings et al. 2011; Geyer and Ralston 2011). The varying parameter space the estuary falls into highlights its large dynamic range and may further explain some of the estuarine exchange variability.

## Exchange Flow Variability

As explained in the “Empirical Orthogonal Functions” section and “Velocity EOFs” section, subtidal-filtered velocity EOFs were computed to examine how the velocity changed over time. The first mode (barotropic-type profile) peaks during periods of high river flow events where the maximum correlation ( $r=0.68$ ,  $p<0.001$ ) occurs when the EOF mode 1 lags discharge measured ~16 km upstream by 7 h. EOF2 (2-layer baroclinic-type profile) correlates well the exchange velocity strength,  $U_E^{obs}$  ( $r=0.91$ ,  $p<0.001$ ).

The exchange flow (in estuaries in steady-state) is expected to be non-linearly dependent on the river flow, ( $u_E^{theory, Q_R} \sim Q_R^m$ ,  $m \approx 1/3$ , although observed values for  $m$  can vary substantially, MacCready and Geyer 2010; Chant et al. 2018; Ralston and Geyer 2019). In LPL, the observed exchange strength does not correlate well with the river flows (testing a range of  $m$ ). The short-lived, episodic nature

of the river flows (due to regional precipitation patterns, small watershed, and a steep hydrograph) likely prevent the estuary from reaching steady-state. Moreover, as discussed above, the estuary seems to transition across different estuary types depending upon the magnitude of freshwater input which may make this relationship break down. Finally, because EOFs are a mathematical tool that do not always accurately separate physical processes, periods of very high river flows (within the top 95th percentile) occasionally create anomalous patterns in higher EOF modes. As such, for some analyses described in this paper, periods of strongest river flows are ignored.

The strength of the exchange flow,  $U_E^{obs}$ , is positive (out-flowing velocities at the surface and inflowing velocities at depth) 91.7% of the time during the open state (excluding high river flows) indicating primarily a classical estuarine circulation (MacCready and Geyer 2010), unlike the inverse hypersaline-driven circulation structure expected in a Mediterranean climate estuary during summer months with little to no freshwater inflow (Hearn and Largier 1997; Largier et al. 2013; Nidzicko and Monismith 2013). This predominantly classical circulation is likely the result of increased urban runoff leading to small freshwater input year-round (White and Greer 2006). Periods with a negative 2nd EOF mode (suggesting inverse estuarine exchange) are more common during summer months, however, the average subtidal density difference between the upstream CTD and the downstream CTD (i.e., the longitudinal density gradient) is weaker, although not inverse ( $-2.86 \text{ kg m}^{-3}$ ), compared to the when the second EOF mode is positive ( $-3.57 \text{ kg m}^{-3}$ ) (Fig. 2d). Moreover, while temperature contributes more to the density structure during the summer, the estuary does not become a thermal estuary; on average 98% of the density variance is explained by salinity, so this estuary’s density remains salinity dominated.

The exchange velocity strength,  $U_E^{obs}$ , is small ( $U_E^{obs} = 0.015 \text{ m s}^{-1}$ ; standard deviation =  $0.0184 \text{ m s}^{-1}$  for open periods without extreme river flow) compared to the range of 0.05 to  $0.3 \text{ m s}^{-1}$  reported in Geyer (2010). Setting aside the temporal variability, the overall strength of  $U_E^{obs}$  falls between  $u_E^{theory}$  estimated using an unstratified estimate for  $v_t$  (e.g., Nezu and Rodi 1986; Geyer and MacCready 2014) and a stratified  $v_t$  estimate (e.g., Ralston et al. 2008; MacCready 2007) incorporated into Eq. 5 as described in the “Exchange Velocity” section. However, as mentioned there, the sensitivity to the  $v_t$  parameterization makes the magnitude comparison challenging. Importantly, the time variability of  $U_E^{obs}$  does not match well with  $u_E^{theory}$  (Fig. 9c–e) as elaborated below.  $u_E^{theory}$  is stronger during neap tides than spring tides as expected with classical estuarine theory (Geyer and Cannon 1982; MacCready and Geyer 2010). However, the observed exchange velocity is strongest in between the spring and neap tides for the entire data set (Fig. 9). There

are a variety of reasons why  $u_E^{theory}$  estimated from Eq. 5 may not match the observed exchange flow, ranging from the calculation method to dynamical reasons. The calculation may suffer from the coarse estimate for the longitudinal density gradient using point measurements of mid-water column density as well as the bulk estimate of the mixing term which may vary significantly over a tidal cycle (e.g., Ralston et al. 2008). Dynamically, the shallow, yet highly variable water depth (Fig. 1) may mean that both internal and free surface hydraulic control could be important during periods of the tidal cycle or season as has been suggested in another ICE (Largier and Taljaard 1991) and found in strongly stratified estuaries (e.g., McKeon et al. 2020; Geyer and Ralston 2011). Additionally, the tidal variability in stratification (Figs. 7b and 8b) and shear (Figs. 7e and 8e) suggests that tidal straining may contribute to the observed exchange flow (e.g., Jay and Musiak 1994, 1996; Burchard and Baumert 1998). Finally, given the magnitude of the tidal range relative to the mean depth, a full analysis in depth-normalized coordinates as completed in Giddings et al. (2014) may be preferable, however, attempts at this approach was highly sensitive to individual tidal cycles.

Ultimately, without firm estimates of  $v_s$ , a magnitude estimate for  $u_E^{theory}$  is unreliable, and the mismatch in temporal variability suggests that the exchange cannot be fully explained by a traditional pressure-friction balance. Splitting the dataset between low and high sill conditions helps elucidate the spring/neap response of the observed exchange flow. When the sill is low (i.e., the estuary is less constricted, open dots Fig. 10), the exchange flow is strongest during neap tide and weakest during the spring tide as theory would suggest (dashed lines Fig. 10). However, when the sill is high (i.e., the estuary is constricted, closed dots Fig. 10), the spring and between spring/neap tide exchange flows are strongest while the neap tide exhibits the weakest exchange (solid lines Fig. 10). This response may be due to tidal pumping or hydraulic control near the sill where, when the sill is very high during ebb tides, the top portion preferentially flows out of the estuary (Largier and Taljaard 1991; Seim and Gregg 1997; Blanton et al. 2000), with stronger outflows during the spring tides. In addition, if during higher sill conditions the flooding tide enters the system more like a density current (Largier et al. 1997, 2013; Nidzioko and Monismith 2013), the net effect of stronger inflows along the bottom and outflows only along the surface during spring tides and overall weaker inflow and outflows during neap tides could contribute to the net higher exchange flow during the spring tides than the neap tides. Ultimately, the data suggests that when the sill is high additional dynamics impact the exchange flow. This is consistent with the very large parameter space that the estuary spans depending on river flow and sill height suggesting that the dynamical drivers of the exchange flow and stratification must also vary over time. However, a lack of velocity and density observations near the sill limits our ability to fully understand the interplay of mechanisms between sill height and spring/neap

tidal conditions that impact the estuarine exchange flow strength. This is an area that needs to be addressed with future observations or a numerical model as the exchange flow is important for the residence time, dispersal of larvae, and mixing of pollutants.

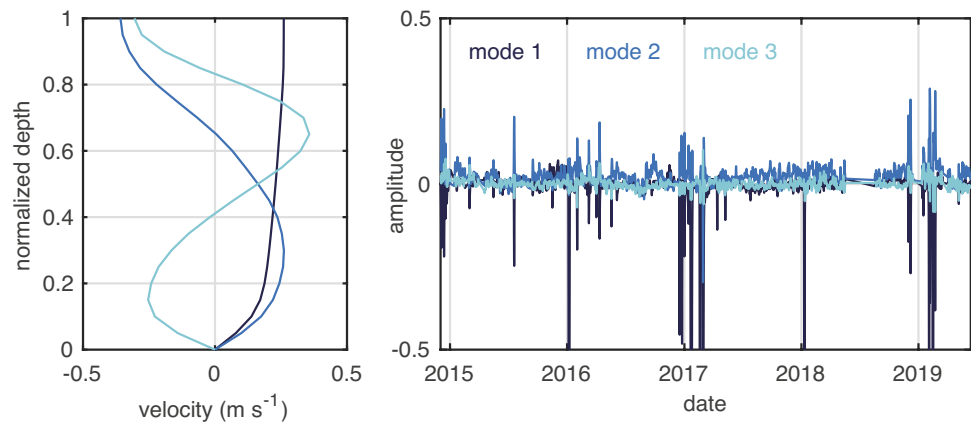
## Conclusions

A total of 4.5 years of observations from Los Peñasquitos Lagoon highlight its large dynamic range over interannual, seasonal, fortnightly, and tidal timescales and its sensitivity to forcing and morphodynamic conditions. While this system would historically have functioned more like a primarily open, low-inflow estuary with periodic inverse estuarine circulation; the main channel density now remains salinity dominated and only occasionally exhibits inverse circulation. Additionally, sill growth and estuary closures have increased, likely due to development in and around the watershed reducing winter freshwater inputs, changing sediment loading, and restricting mouth migration (e.g., White and Greer 2006; Hastings and Elwany 2012). When the sill near the mouth is low, the estuary functions, in many ways, like a larger, classical estuary with evidence of strain-induced period stratification and a classical exchange flow that is larger during neap tides, consistent with theory. A combination of flood dominance, wave-current-water level interactions leading to preferential IG wave propagation during flood tides, and wave-induced sediment transport contribute to inlet accretion and sill growth. As the sill grows, the estuarine exchange strengthens, particularly during spring tides, thereby departing from classical estuarine theory. The departure from theory when the sill is high suggests processes other than the baroclinic density gradients are contributing to the subtidal exchange. Intratidal variations in mixing are present and likely contribute, but it is also possible that internal and free surface hydraulic control and/or wave dynamics at the mouth may play a role—areas which require further research. As has been shown in other LIEs, sill growth and closure is also associated with estuary freshening and potentially deleterious ecosystem consequences including low dissolved oxygen at depth, development of mosquito breeding grounds, and type conversion from salt to freshwater marsh (often with a concomitant increase in invasive species) (e.g., Crooks et al. 2016). These systems are ubiquitous around the world in Mediterranean climates. Given their prevalence, sensitivity to forcing conditions, rapid morphological alterations, large dynamic range, and important ecosystem services, their continuous observation is necessary to understand how their dynamics might be expected to change under future climate conditions.

## Appendix EOF Calculations

The velocity EOFs described in the “Velocity EOFs” section are included here for clarity. Figure 11 includes the shapes and time series amplitudes for the first three EOF modes. Figure 12

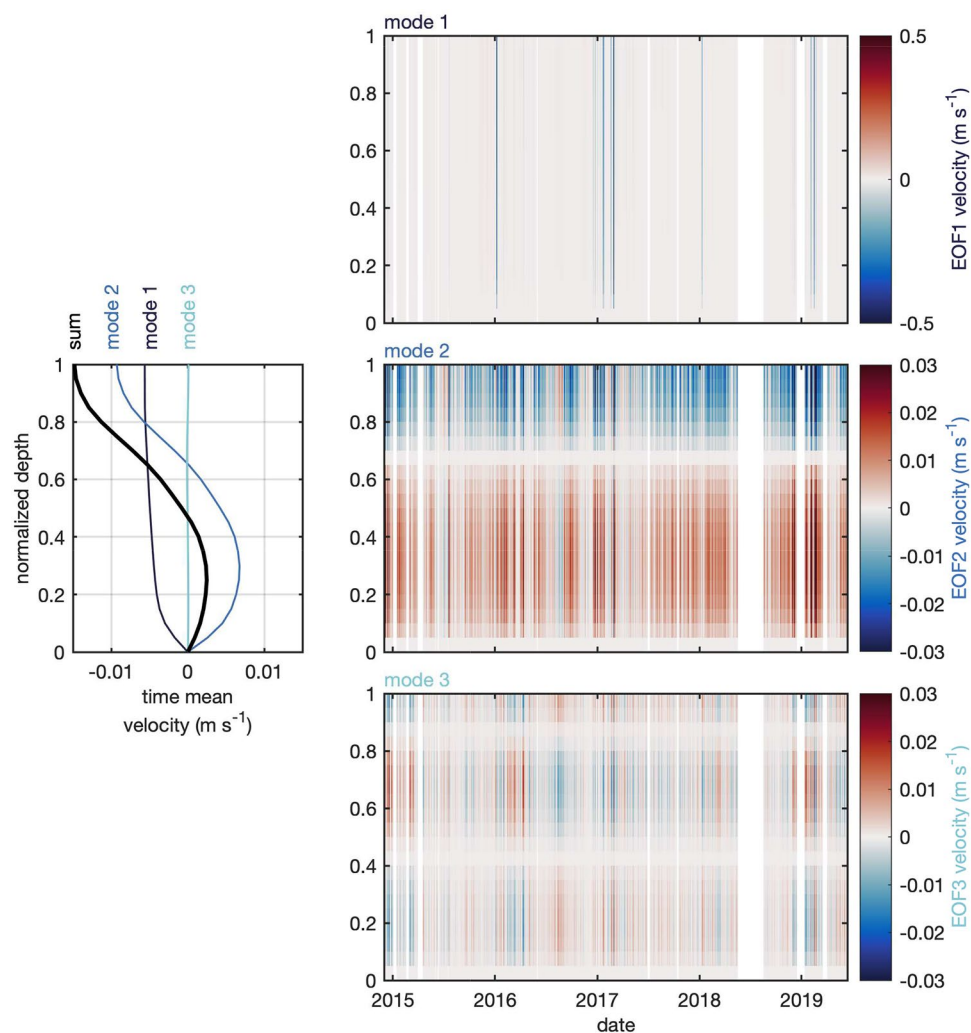
**Fig. 11** EOF vertical profile shapes (left) and time series amplitudes (right) for the first 3 EOF modes. As a reminder, these EOFs are singular value decomposition (SVD) (Thomson and Emery 2014) applied to the subtidal (low-passed) velocities. The first 3 EOF modes of the 1-h interpolated residual velocities for all available data explain 94.0%, 5.1%, and 0.01% of the total velocity variance, respectively



includes a re-construction of the first three EOF mode velocities over time and depth and the time mean over depth. As noted in the “Velocity EOFs” section, mode 1 resembles a barotropic flow profile and is nearly always directed out of the estuary. EOF1 includes a few amplitude peaks during periods of large river flow. The time mean of the EOF1 velocity is out of the estuary with a magnitude reasonable for a mean riverine outflow.

EOF mode 2 exhibits a 2-layer sheared profile similar to a baroclinic structure and is in the direction expected for classical estuarine circulation (into the estuary at depth, out at the surface) for most of the time series (and for the time mean) with a few exceptions during the summer months and during closures. EOF3 is much smaller than the other two modes and the time mean profile is essentially zero.

**Fig. 12** EOF re-constructed velocities for the first 3 EOF modes. Velocity profiles over time re-constructed for modes 1–3 (right) and averaged over all 4.5 years (left). Note that mode 1 is typically small but experiences values much greater than mode 2 during large events. Mode 2 is almost always into the estuary at depth and out at the surface as expected for estuarine gravitational circulation. The time mean of each mode on the left shows the dominance of modes 1 and 2



**Acknowledgements** We thank members and volunteers of the Giddings, Guza, and Pawlak labs at UCSD (esp. Angelica Rodriguez and Isabella Arzeno), the Center for Coastal Studies field crew (esp. Michele Okihiro, Brian Woodward, and Greg Boyd), and the scientists at the Tijuana River National Estuarine Research Reserve (esp. Justin McCullough) for help with data collection. We thank the Los Peñasquitos Lagoon Foundation (esp. Mike Hastings) and California State Parks (esp. Cara Stafford, Darren Smith, and Reinhard Flick) for helping to facilitate this research, invaluable insights, and providing permits. Additionally, we would like to thank John Largier and members of the Giddings, Pawlak, Merrifield, Feddersen, and Guza labs at SIO for helpful discussions and suggestions. Finally, we would like to thank 2 anonymous reviewers and the editor for very helpful feedback which helped to improve this manuscript. This work was partially funded by University of Southern California Sea Grant grants #75193327 and #61207777 with Scripps Institution of Oceanography (SIO), California (CA) Department of Parks and Recreation Division of Boating and Waterways Oceanography Program under contract #C1670005 with SIO, NOAA's National Centers for Coastal Ocean Science (NCCOS) Competitive Research Program under award NA18NOS4780172 to SIO and award NA16NOS4780205 to the CA Coastal Conservancy, National Science Foundation project OCE-1924005, NOAA's Office for Coastal Management, and the CA Coastal Conservancy's support of long-term monitoring conducted by the Tijuana River NERR as part of the Los Peñasquitos Lagoon Enhancement Plan. This is CHRP Contribution 248. This work was additionally supported by two traineeships through University of Southern California Sea Grant. Supplemental data were collected from NOAA, CDIP, SCCOOS, USGS, Earth Networks, Inc., and the TRNERR SWMP.

**Open Access** This article is licensed under a Creative Commons Attribution 4.0 International License, which permits use, sharing, adaptation, distribution and reproduction in any medium or format, as long as you give appropriate credit to the original author(s) and the source, provide a link to the Creative Commons licence, and indicate if changes were made. The images or other third party material in this article are included in the article's Creative Commons licence, unless indicated otherwise in a credit line to the material. If material is not included in the article's Creative Commons licence and your intended use is not permitted by statutory regulation or exceeds the permitted use, you will need to obtain permission directly from the copyright holder. To view a copy of this licence, visit <http://creativecommons.org/licenses/by/4.0/>.

## References

- Bagnold, R.A. 1966. An approach to the sediment transport problem from general physics. *USGS Report* 422: 11–137. <https://doi.org/10.3133/pp422i>.
- Barnard, P.L., D. Hoover, D.M. Hubbard, A. Snyder, B.C. Ludka, J. Allan, G.M. Kaminsky, P. Ruggiero, T.W. Gallien, L. Gabel, D. McCandless, H.M. Weiner, N. Cohn, D.L. Anderson, and K.A. Serafin. 2017. Extreme oceanographic forcing and coastal response due to the 2015–2016 El Niño. *Nature Communications* 8: 14365. <https://doi.org/10.1038/ncomms14365>.
- Behrens, D.K., F.A. Bombardelli, and J.L. Largier. 2016. Landward propagation of saline waters following closure of a bar-built estuary: Russian River (California, USA). *Estuaries and Coasts* 39: 621–638. <https://doi.org/10.1007/s12237-015-0030-8>.
- Behrens, D.K., F.A. Bombardelli, J.L. Largier, and E. Twohy. 2013. Episodic closure of the tidal inlet at the mouth of the Russian River — A small bar-built estuary in California. *Geomorphology* 189: 66–80. <https://doi.org/10.1016/j.geomorph.2013.01.017>.
- Beller, E.E., S.A. Baumgarten, R.M. Grossinger, T.R. Longcore, E.D. Stein, S.J. Dark, and S.R. Dusterhoff. 2014. Northern San Diego County lagoons historical ecology investigation: regional patterns, local diversity, and landscape trajectories. Prepared for the State Coastal Conservancy. SFEI Publication #722, San Francisco Estuary Institute, Richmond, CA.
- Bertin, X., A. de Bakker, A. van Dongeren, G. Coco, G. André, F. Ardhuin, P. Bonneton, F. Bouchette, B. Castelle, W.C. Crawford, M. Davidson, M. Deen, G. Dodet, T. Guérin, K. Inch, F. Leckler, R. McCall, H. Muller, M. Olabarrieta, D. Roelvink, G. Ruessink, D. Sous, E. Stutzmann, and M. Tissier. 2018. Infragravity waves: From driving mechanisms to impacts. *Earth-Science Reviews* 177: 774–799. <https://doi.org/10.1016/j.earscirev.2018.01.002>.
- Bertin, X., D. Mendes, K. Martins, A.B. Fortunato, and L. Lavaud. 2019. The closure of a shallow tidal inlet promoted by infragravity waves. *Geophysical Research Letters* 46: 6804–6810. <https://doi.org/10.1029/2019gl083527>.
- Bertin, X., and M. Olabarrieta. 2016. Relevance of infragravity waves in a wave-dominated inlet. *Journal of Geophysical Research: Oceans* 121: 5418–5435. <https://doi.org/10.1002/2015jc011444>.
- Blanton, J.O., M.A. Ferreira, and F.A. Andrade. 2000. Effect of a broad shallow sill on tidal circulation and salt transport in the entrance to a coastal plain estuary (Mira—Vila Nova de Milfontes, Portugal). *Estuaries* 23: 293–304. <https://doi.org/10.2307/1353322>.
- Bond, N.A., M.F. Cronin, H. Freeland, and N. Mantua. 2015. Causes and impacts of the 2014 warm anomaly in the NE Pacific. *Geophysical Research Letters* 42: 3414–3420. <https://doi.org/10.1002/2015GL063306>.
- Burchard, H., and H. Baumert. 1998. The formation of estuarine turbidity maxima due to density effects in the salt wedge. A hydrodynamic process study. *Journal of Physical Oceanography* 28: 309–321. [https://doi.org/10.1175/1520-0485\(1998\)028%3c0309:TFOETM%3e2.0.CO;2](https://doi.org/10.1175/1520-0485(1998)028%3c0309:TFOETM%3e2.0.CO;2).
- Bouma, T.J., J. van Belzen, T. Balke, Z. Zhu, L. Airoldi, A.J. Blight, A.J. Davies, C. Galvan, S.J. Hawkins, S.P.G. Hoggart, J.L. Lara, I.J. Losada, M. Maza, B. Ondiviela, M.W. Skov, E.M. Strain, R.C. Thompson, S. Yang, B. Zanuttigh, L. Zhang, and P.M.J. Herman. 2014. Identifying knowledge gaps hampering application of intertidal habitats in coastal protection: Opportunities & steps to take. *Coastal Engineering* 87: 147–157. <https://doi.org/10.1016/j.coastaleng.2013.11.014>.
- Chant, R.J., C.K. Sommerfield, and S.A. Talke. 2018. Impact of channel deepening on tidal and gravitational circulation in a highly engineered estuarine basin. *Estuaries and Coasts* 41: 1587–1600. <https://doi.org/10.1007/s12237-018-0379-6>.
- Clark, R., and K. O'Connor. 2019. A systematic survey of bar-built estuaries along the California coast. *Estuarine, Coastal and Shelf Science* 226: 106285. <https://doi.org/10.1016/j.ecss.2019.106285>.
- Cole, K.L., and E. Wahl. 2000. A Late Holocene paleoecological record from Torrey Pines State Reserve, California. *Quaternary Research* 53: 341–351. <https://doi.org/10.1006/qres.1999.2121>.
- Cooper, J.A.G. 2001. Geomorphological variability among microtidal estuaries from the wave-dominated South African coast. *Geomorphology* 40: 99–122. [https://doi.org/10.1016/s0169-555x\(01\)00039-3](https://doi.org/10.1016/s0169-555x(01)00039-3).
- Cousins, M., M.T. Stacey, and J.L. Drake. 2010. Effects of seasonal stratification on turbulent mixing in a hypereutrophic coastal lagoon. *Limnology and Oceanography* 55: 172–186. <https://doi.org/10.4319/lo.2010.55.1.0172>.
- Crooks, J.A., D.M. Talley, M. Cordrey, C. Whitcraft, J. Lorda-Solorzano, K. Uyeda, H. Bellringer, J. McCullough, and M. Almeida. 2016. Unnatural history: Biological invasions into coastal ecosystems. In *Proceedings of the US-Iran Symposium on Wetlands*: 193–203, Irvine, California.
- Crooks, J.A., J. McCullough, H. Bellringer, and M. Cordrey. 2014. The physical, chemical and biological monitoring of Los Peñasquitos Lagoon. Annual Report.
- Davidson, M.A., B.D. Morris, and I.L. Turner. 2009. A simple numerical model for inlet sedimentation at intermittently open–closed coastal

- lagoons. *Continental Shelf Research* 29: 1975–1982. <https://doi.org/10.1016/j.csr.2008.10.005>.
- Dodet, G., X. Bertin, N. Bruneau, A.B. Fortunato, A. Nahon, and A. Roland. 2013. Wave-current interactions in a wave-dominated tidal inlet. *Journal of Geophysical Research: Oceans* 118: 1587–1605. <https://doi.org/10.1002/jgrc.20146>.
- Dronkers, J. 1986. Tidal asymmetry and estuarine morphology. *Netherlands Journal of Sea Research* 20: 117–131.
- Dussaillant, A., P. Galdames, and C. Sun. 2009. Water level fluctuations in a coastal lagoon: El Yali Ramsar wetland, Chile. *Desalination* 246: 202–214. <https://doi.org/10.1016/j.desal.2008.03.053>.
- Elwany, H. 2011. Characteristics, restoration, and enhancement of Southern California Lagoons. *Journal of Coastal Research* 59: 246–255. <https://doi.org/10.2112/si59-026.1>.
- Friedrichs, C.T., and O.S. Madsen. 1992. Nonlinear diffusion of the tidal signal in frictionally dominated embayments. *Journal of Geophysical Research: Oceans* 97: 5637–5650. <https://doi.org/10.1029/92JC00354>.
- Gale, E., C. Pattiaratchi, and R. Ranasinghe. 2006. Vertical mixing processes in intermittently closed and open lakes and lagoons, and the dissolved oxygen response. *Estuarine, Coastal and Shelf Science* 69: 205–216. <https://doi.org/10.1016/j.ecss.2006.04.013>.
- Gale, E., C. Pattiaratchi, and R. Ranasinghe. 2007. Processes driving circulation, exchange and flushing within intermittently closing and opening lakes and lagoons. *Marine and Freshwater Research* 58: 709–719. <https://doi.org/10.1071/MF06121>.
- Geyer, R.W., and P. MacCready. 2014. The estuarine circulation. *Fluid Mechanics* 46: 175–197. <https://doi.org/10.1146/annurev-fluid-010313-141302>.
- Geyer, W.R. 2010. Estuarine salinity structure and circulation: 12–26. <https://doi.org/10.1017/cbo9780511676567.003>.
- Geyer, W.R., and D.K. Ralston. 2011. The dynamics of strongly stratified estuaries. In *Treatise on Estuarine and Coastal Science*: 2: 37–52 Elsevier Inc. <https://doi.org/10.1016/b978-0-12-374711-2.00206-0>.
- Geyer, W.R., and G.A. Cannon. 1982. Sill processes related to deep water renewal in a fjord. *Journal of Geophysical Research: Oceans* 87: 7985–7996. <https://doi.org/10.1029/jc087ic10p07985>.
- Giddings, S.N., D.A. Fong, and S. Monismith. 2011. Role of straining and advection in the intratidal evolution of stratification, vertical mixing, and longitudinal dispersion of a shallow, macrotidal, salt wedge estuary. *Journal of Geophysical Research* 116: C03003. <https://doi.org/10.1029/2010JC006482>.
- Giddings, S.N., G. Monismith, D.A. Fong, and M.T. Stacey. 2014. Using depth-normalized coordinates to examine mass transport residual circulation in estuaries with large tidal amplitude relative to the mean depth. *Journal of Physical Oceanography* 44: 128–148. <https://doi.org/10.1175/jpo-d-12-0201.1>.
- Godin, G. 1972. The analysis of tides: University of Toronto Press, 264 pp.
- Goodman, A.C., K.M. Thorne, K.J. Buffington, C.M. Freeman, and C.N. Janousek. 2018. El Niño increases high-tide flooding in tidal wetlands along the U.S. Pacific Coast. *Journal of Geophysical Research: Biogeosciences* 123: 3162–3177. <https://doi.org/10.1029/2018JG004677>.
- Hansen, D.V., and M. Rattray. 1966. New dimensions in estuary classification. *Limnology and Oceanography* 11: 319–326. <https://doi.org/10.2307/2833361>.
- Hartmann, D.L. 2015. Pacific sea surface temperature and the winter of 2014. *Geophysical Research Letters* 42: 1894–1902. <https://doi.org/10.1002/2015GL063083>.
- Harvey, M.E., S.N. Giddings, E. Stein, J.A. Crooks, C. Whitcraft, T. Gallien, J.L. Largier, L. Tiefenthaler, H. Meltzer, G. Pawlak, K. Thorne, K. Johnston, R. Ambrose, S.C. Schroeter, H.M. Page, and H. Elwany. 2020. Effects of elevated sea levels and waves on Southern California estuaries during the 2015–2016 El Niño. *Estuaries and Coasts*. <https://doi.org/10.1007/s12237-019-00676-1>.
- Hastings, M., and H. Elwany. 2012. Managing the inlet at Los Peñasquitos Lagoon. *Shore and Beach* 80: 2012.
- Hayes, M.O. 1979. Barrier island morphology as a function of tidal wave and wave regime. In *Barrier Islands from Mexico to the Gulf of St. Lawrence*: 1–28. Academic Press.
- Hearn, C.J., and J. Largier. 1997. The summer buoyancy dynamics of a shallow Mediterranean estuary and some effects of changing bathymetry; Tomales Bay, California. *Estuarine, Coastal and Shelf Sciences* 45: 497–506.
- Henning, C., C. Loflen, D. Jayne, L. Honma, C. Cheng, W. Chiu, C. Gorham, and B. Tobler. 2012. Sediment TMDL for Los Peñasquitos Lagoon.
- Holmquist, J.R., L. Windham-Myers, N. Bliss, S. Crooks, J.T. Morris, J.P. Megonigal, T. Troxler, D. Weller, J. Callaway, J. Drexler, M.C. Ferner, M.E. Gonnee, K.D. Kroeger, L. Schile-Beers, I. Woo, K. Buffington, J. Breithaupt, B.M. Boyd, L.N. Brown, N. Dix, L. Hice, B.P. Horton, G.M. MacDonald, R.P. Moyer, W. Reay, T. Shaw, E. Smith, J.M. Smoak, C. Sommerfield, K. Thorne, D. Velinsk, E. Watson, K. Wilson Grimes, and M. Woodrey. 2018. Accuracy and precision of tidal wetland soil carbon mapping in the conterminous United States. *Science and Reports* 8: 9478. <https://doi.org/10.1038/s41598-018-26948-7>.
- Jay, D.A., and J.D. Musiak. 1994. Particle trapping in estuarine tidal flows. *Journal of Geophysical Research*:99(C10): 20445–20461. <https://doi.org/10.1029/94JC00971>.
- Jay, D.A., and Musiak, J.D., 1996. Internal tidal asymmetry in channel flows: Origins and consequences. *Coastal and Estuarine Studies*: 211–249. <https://doi.org/10.1029/CE050p0211>.
- Largier, J., K. O'Connor, and R. Clark. 2019. Considerations for Management of the Mouth State of California's Bar-Built Estuaries. Report to the Pacific States Marine Fisheries Commission and NOAA (NA14NMF437012).
- Largier, J.L. 1986. Structure and mixing in the Palmiet Estuary, South Africa. *South African Journal of Marine Science* 4: 139–152. <https://doi.org/10.2989/025776186784461729>.
- Largier, J.L. 2010. Low inflow estuaries: hypersaline, inverse, and thermal scenarios. Contemporary issues in estuarine physics. *Cambridge: Cambridge University Press*. <https://doi.org/10.1017/CBO9780511676567>.
- Largier, J.L., C.J. Hearn, and B.D. Chadwick. 2013. Density structures in “low inflow estuaries.” In *Buoyancy Effects on Coastal and Estuarine Dynamics*, eds D.G. Aubrey and C. Friedrichs). Wiley. <https://doi.org/10.1029/CE053p0227>.
- Largier, J. L., J.H. Slinger, and S. Taljaard. 1992. The stratified hydrodynamics of the Palmiet - A prototypical bar-built estuary. In *Dynamics and Exchanges in Estuaries and the Coastal Zone*, 135–153. American Geophysical Union. <https://doi.org/10.1029/ce040p0135>.
- Largier, J.L., J.T. Hollibaugh, and S.V. Smith. 1997. Seasonally hypersaline estuaries in mediterranean-climate regions. *Estuarine, Coastal and Shelf Science* 45 (789): 797.
- Largier, J.L., and S. Taljaard. 1991. The dynamics of tidal intrusion, retention, and removal of seawater in a bar-built estuary. *Estuarine, Coastal and Shelf Science* 33: 325–338. [https://doi.org/10.1016/0272-7714\(91\)90061-f](https://doi.org/10.1016/0272-7714(91)90061-f).
- Los Peñasquitos Foundation, ESA, KTUA, and Norby Consulting. 2016. Los Peñasquitos Lagoon Enhancement Plan.
- Ludka, B.C., T.W. Gallien, S.C. Crosby, and R.T. Guza. 2016. Mid-El Niño erosion at nourished and unnourished Southern California beaches. *Geophysical Research Letters* 43: 4510–4516. <https://doi.org/10.1002/2016GL068612>.
- MacCready, P. 2007. Estuarine adjustment. *Journal of Physical Oceanography* 37 (8): 2133–2145. <https://doi.org/10.1175/JPO3082.1>.
- MacCready, P., and R.W. Geyer. 2010. Advances in Estuarine Physics. *Annual Review of Marine Science* 2: 35–58. <https://doi.org/10.1146/annurev-marine-120308-08101>.

- McKeon, M.A., A.R. Horner-Devine, and S.N. Giddings. 2020. Seasonal changes in structure and dynamics in an urbanized salt wedge estuary. *Estuaries and Coasts*. <https://doi.org/10.1007/s12237-020-00788-z>.
- McSweeney, S.L., D.M. Kennedy, I.D. Rutherford, and J.C. Stout. 2017. Intermittently closed/open lakes and lagoons: Their global distribution and boundary conditions. *Geomorphology* 292: 142–152. <https://doi.org/10.1016/j.geomorph.2017.04.022>.
- McSweeney, S.L., J.C. Stout, and D.M. Kennedy. 2020. Variability in infragravity wave processes during estuary artificial entrance openings. *Earth Surf. Process. Landforms* 45: 3414–3428. <https://doi.org/10.1002/esp.4974>.
- Moreno, I., A. Ávila, and M. Losada. 2010. Morphodynamics of intermittent coastal lagoons in Southern Spain: Zahara de los Atunes. *Geomorphology* 121: 305–316. <https://doi.org/10.1016/j.geomorph.2010.04.028>.
- Nezu, I., and W. Rodi. 1986. Open-channel flow measurements with a laser doppler anemometer. *Journal of Hydraulic Engineering* 112 (5): 335–355. [https://doi.org/10.1061/\(ASCE\)0733-9429\(1986\)112:5\(335\)](https://doi.org/10.1061/(ASCE)0733-9429(1986)112:5(335)).
- Nidziko, N.J. 2010. Tidal asymmetry in estuaries with mixed semi-diurnal/diurnal tides. *Journal of Geophysical Research: Oceans* 115. <https://doi.org/10.1029/2009JC005864>.
- Nidziko, N.J., and D.K. Ralston. 2012. Tidal asymmetry and velocity skew over tidal flats and shallow channels within a macrotidal river delta. *Journal of Geophysical Research: Oceans*: 117. <https://doi.org/10.1029/2011JC007384>.
- Nidziko, N.J., and S.G. Monismith. 2013. Contrasting seasonal and fortnightly variations in the circulation of a seasonally inverse estuary, Elkhorn Slough, California. *Estuaries and Coasts* 36: 1–17. <https://doi.org/10.1007/s12237-012-954-1>.
- Olabarrieta, M., J.C. Warner, and N. Kumar. 2011. Wave-current interaction in Willapa Bay. *Journal of Geophysical Research: Oceans* 116. <https://doi.org/10.1029/2011JC007387>.
- Orescanin, M., B. Raubenheimer, and S. Elgar. 2014. Observations of wave effects on inlet circulation. *Continental Shelf Research* 34: 37–42. <https://doi.org/10.1016/j.csr.2014.04.010>.
- Orescanin, M.M., and J. Scooler. 2018. Observations of episodic breaching and closure at an ephemeral river. *Continental Shelf Research* 166: 77–82. <https://doi.org/10.1016/j.csr.2018.07.003>.
- Purer, E.A. 1942. Plant ecology of the coastal salt marshlands of San Diego County, California. *Ecological Monographs* 12: 81–111.
- Ralston, D.K., and R.W. Geyer. 2019. Response to channel deepening of the salinity intrusion, estuarine circulation, and stratification in an urbanized estuary. *Journal of Geophysical Research: Oceans*. <https://doi.org/10.1029/2019JC015006>.
- Ralston, D.K., R.W. Geyer, and J.A. Lerczak. 2008. Subtidal salinity and velocity in the Hudson River Estuary: Observations and modeling. *Journal of Physical Oceanography* 38: 753–770. <https://doi.org/10.1175/2007jpo3808>.
- Ralston, D.K., W.R. Geyer, and J.A. Lerczak. 2010. Structure, variability, and salt flux in a strongly forced salt wedge estuary. *Journal of Geophysical Research: Oceans* 115 (C6). <https://doi.org/10.1029/2009JC005806>.
- Ranasinghe, R., and C. Pattiaratchi. 1999a. The seasonal closure of tidal inlets: Wilson Inlet—A case study. *Coastal Engineering* 37: 37–56. [https://doi.org/10.1016/s0378-3839\(99\)00007-1](https://doi.org/10.1016/s0378-3839(99)00007-1).
- Ranasinghe, R., and C. Pattiaratchi. 1999b. Circulation and mixing characteristics of a seasonally open tidal inlet: A field study. *Marine and Freshwater Research* 50: 281–290. <https://doi.org/10.1071/mf98037>.
- Ranasinghe, R., and C. Pattiaratchi. 2003. The seasonal closure of tidal inlets: Causes and effects. *Coastal Engineering Journal* 45: 601–627. <https://doi.org/10.1142/S0578563403000919>.
- Ranasinghe, R., C. Pattiaratchi, and G. Masselink. 1999. A morphodynamic model to simulate the seasonal closure of tidal inlets. *Coastal Engineering* 37: 1–36. [https://doi.org/10.1016/s0378-3839\(99\)00008-3](https://doi.org/10.1016/s0378-3839(99)00008-3).
- Raubenheimer, B., S. Elgar, and R.T. Guza. 1998. Estimating wave heights from pressure measured in sand Bed. *Journal of Waterway, Port, Coastal, and Ocean Engineering* 124: 151–154. [https://doi.org/10.1061/\(asce\)0733-950x\(1998\)124:3\(151\)](https://doi.org/10.1061/(asce)0733-950x(1998)124:3(151)).
- Rezaie, A.M., J. Loerzel, and C.M. Ferreira. 2020. Valuing natural habitats for enhancing coastal resilience: Wetlands reduce property damage from storm surge and sea level rise. *PLoS ONE* 15 (1): e0226275. <https://doi.org/10.1371/journal.pone.0226275>.
- Rich, A., and E.A. Keller. 2013. A hydrologic and geomorphic model of estuary breaching and closure. *Geomorphology* 191: 64–74. <https://doi.org/10.1016/j.geomorph.2013.03.003>.
- Roy, P.S., R.J. Williams, A.R. Jones. 2001. Structure and function of south-east Australian estuaries. *Estuarine Coastal and Shelf Science*: 53. <https://doi.org/10.1006/escs.2001.0796>.
- SANDAG. 2018. Regional Monitoring Report.
- Scott, D.B., P.J. Mudie, and J.S. Bradshaw. 2011. Coastal evolution of Southern California as interpreted from benthic foraminifera, ostracodes, and pollen. *Journal of Foraminiferal Research* 41 (285): 307.
- Seim, H.E., and M.C. Gregg. 1997. The importance of aspiration and channel curvature in producing strong vertical mixing over a sill. *Journal of Geophysical Research: Oceans* 102: 3451–3472. <https://doi.org/10.1029/96jc03415>.
- Shepard, C.C., C.M. Crain, and M.W. Beck. 2011. The protective role of coastal marshes: A systematic review and meta-analysis. *PLoS ONE* 6 (11): e27374. <https://doi.org/10.1371/journal.pone.0027374>.
- Siler, N., Y. Kosaka, S. Xie, and X. Li. 2017. Tropical ocean contributions to California's surprisingly dry El Niño of 2015/16. *Journal of Climate* 30: 10067–10079. <https://doi.org/10.1175/JCLI-D-17-0177.1>.
- Simpson, J.H., J. Brown, J. Matthews, and G. Allen. 1990. Tidal straining, density currents, and stirring in the control of estuarine stratification. *Estuaries* 13: 125–132. <https://doi.org/10.2307/1351581>.
- Stacey, M.T., J.R. Burau, and S.G. Monismith. 2001. Creation of residual flows in a partially stratified estuary. *Journal of Geophysical Research*: 106(C8): 17013–17037. <https://doi.org/10.1029/2000JC000576>.
- Thompson, R.O.R.Y. 1983. Low-pass filters to suppress inertial and tidal frequencies. *Journal of Physical Oceanography* 13 (6): 1077–1083. [https://doi.org/10.1175/1520-0485\(1983\)013%3c1077:LPFTSI%3e2.0.CO;2](https://doi.org/10.1175/1520-0485(1983)013%3c1077:LPFTSI%3e2.0.CO;2).
- Thomson, R.E., and W.J. Emery. 2014. Data analysis methods in physical oceanography (Third Edition): 593–637. <https://doi.org/10.1016/b978-0-12-387782-6.00006-5>.
- Uncles, R.J., J.A. Stephens, and C. Harris. 2014. Freshwater, tidal and wave influences on a small estuary. *Estuarine, Coastal and Shelf Science* 150: 252–261. <https://doi.org/10.1016/j.ecss.2014.05.035>.
- Walters, R.A., and C. Heston. 1982. Notes and correspondence: Removing tidal-period variations from time-series data using low-pass digital filters. *Journal of Physical Oceanography*: 12.
- White, M.D., and K.A. Greer. 2006. The effects of watershed urbanization on the stream hydrology and riparian vegetation of Los Peñasquitos Creek, California. *Landscape and Urban Planning* 74: 125–138. <https://doi.org/10.1016/j.landurbplan.2004.11.015>.
- Williams, M.E. 2014. Hydrodynamics and salt dispersion in intermittently closed bar-built estuaries: UC Berkeley. ProQuest ID: Williams\_berkeley\_0028E\_14663. Merritt ID: ark:/13030/m5gf5q9t. Retrieved from <https://escholarship.org/uc/item/4h3770rr>.
- Williams, M.E., and M.T. Stacey. 2016. Tidally discontinuous ocean forcing in bar-built estuaries: The interaction of tides, infragravity motions, and frictional control. *Journal of Geophysical Research: Oceans* 121: 571–585. <https://doi.org/10.1002/2015jc011166>.
- Winant, C.D., and G.G. de Velasco. 2003. Tidal dynamics and residual circulation in a well-mixed inverse estuary. *Journal of Physical*

- Oceanography* 33 (7): 1365–1379. [https://doi.org/10.1175/1520-0485\(2003\)033%3C1365:TDARCI%3E2.0.CO;2](https://doi.org/10.1175/1520-0485(2003)033%3C1365:TDARCI%3E2.0.CO;2).
- Young, A.P., R.E. Flick, T.W. Gallien, S.N. Giddings, R.T. Guza, M. Harvey, B.C. Luc Lenain, KW Melville, Ludka, and W.C. O'Reilly. 2018. Southern California Coastal Response to the 2015–2016 El Niño. *Journal of Geophysical Research: Earth Surface* 123: 3069–3083. <https://doi.org/10.1029/2018JF004771>.
- Zedler, J.B., and S. Kercher. 2005. Wetland resources: Status, trends, ecosystem services, and restorability. *Annual Review of Environment and Resources* 30: 39–74. <https://doi.org/10.1146/annurev.energy.30.050504.144248>.